

Active Impedance Matching and Sensitivity Optimized
Phased Array Feed Design For Radio Astronomy

David E. Carter

A thesis submitted to the faculty of
Brigham Young University
in partial fulfillment of the requirements for the degree of
Master of Science

Karl F. Warnick, Chair
Brian D. Jeffs
Michael A. Jensen

Department of Electrical Engineering
Brigham Young University
December 2011

Copyright © 2011 David E. Carter
All Rights Reserved

ABSTRACT

Active Impedance Matching and Sensitivity Optimized Phased Array Feed Design For Radio Astronomy

David E. Carter
Department of Electrical Engineering, BYU
Master of Science

One of the many challenges in radio astronomy is the ability to make accurate measurements quickly. In recent years engineers and astronomers have begun implementing phased array feeds (PAFs) as a way to negate the long observation times required by single antenna feeds. Unfortunately, large mutual coupling and other loss terms result in low sensitivity, restricting PAF usefulness in on dish observation. This thesis addresses several ways to reduce mutual coupling and maximize sensitivity for PAFs in radio astronomy.

Antenna design of this magnitude requires accurate modeling capabilities. To this end, electromagnetic software models and low loss component designs are verified and validated with measured data. This process required the construction of a 50Ω matched dipole and measurements on a network analyzer at Brigham Young University.

The design and optimization of several single and dual polarization hexagonal grid arrays of 19 and 38 elements respectively are also described. Model figures of merit are compared with measurements taken on the 20-Meter dish at the National Radio Astronomy Observatory (NRAO) in Green Bank, WV and the 300 meter dish at the Arecibo Observatory in Arecibo, PR. Although some unexplained discrepancies exist between measured and model datasets, the dual pol cryo-cooled kite array described boasts the highest PAF sensitivity ever measured.

Keywords: Karl Jansky, National Radio Astronomy Observatory, Arecibo Observatory, phased array feed, active impedances, beamforming

ACKNOWLEDGMENTS

I would like to thank several individuals for their help and support. Dr. Karl Warnick and Dr. Brian Jeffs for their dedication, leadership, and guidance. Dr. Rick Fisher and Roger Norrod from NRAO as well as Ganesh Rajagopalan and the staff at Arecibo Observatory for their time and assistance with experimental setup and data collection. Also, my friends and fellow students at BYU for their aid and good humor. Finally, I would like to thank my wife Sarah and daughter Danielle (Bug) for their patience and support throughout.

TABLE OF CONTENTS

LIST OF TABLES	ix
LIST OF FIGURES	xi
Chapter 1 Introduction	1
1.1 Radio Astronomy	1
1.2 Phased Arrays in Radio Astronomy	1
1.3 Thesis Contributions	2
1.4 Thesis Outline	3
Chapter 2 Background	5
2.1 Signal Model	5
2.1.1 Beamformers	7
2.2 Active Impedances	8
2.3 Figures of Merit	10
2.3.1 Radiation Efficiency	10
2.3.2 Aperture Efficiency	10
2.3.3 Spillover Efficiency	12
2.3.4 System, Receiver, and LNA Noise Temperatures	12
2.3.5 Sensitivity	14
2.4 BYU Radio Astronomy Receiver Specifications	15
2.5 Hot-Cold Y-factor Technique	15
2.5.1 Single Channel Equivalent Temperatures	17
2.6 Table of Antennas	18
Chapter 3 Model Validation	21
3.1 PAF Design Goals	21
3.2 Thin Dipole Array	21
3.3 Single Element 50 Ω Match	23
3.4 Summary	27
Chapter 4 Single Polarization Array Feed Design	29
4.1 Single Polarization Phased Array Feed	29
4.1.1 The ‘Post’ Design	29
4.1.2 The ‘Kite’ Design	30
4.1.3 The Green Bank Balun Design	30
4.2 Active Impedance Matched Array Design Technique	31
4.3 Modeled and Measured Return Loss	33
4.4 Noise Temperature Comparisons and Hot-Cold Measurements	36
4.4.1 System Noise Temperatures and Efficiencies	38
4.4.2 Hot-Cold Measurements	40
4.5 On Dish Array Characterization	41

4.5.1	Arecibo Phased Array Feasibility Study	41
4.5.2	20-Meter On Dish Measurements	43
4.5.3	Model and On Dish Comparisons	45
4.6	Summary	50
Chapter 5	Dual Polarization Array Feed Design	53
5.1	Infinite Array Model and the Matlab Optimizer	53
5.1.1	Increasing Modeling Efficiency and the Infinite Array Model	54
5.1.2	The Matlab Optimizer	55
5.2	Dual Polarization Element Designs	56
5.2.1	Spline Dipoles	57
5.2.2	Ear Dipoles	57
5.2.3	Cryo Kite Dipoles	60
5.3	Experimental Results	60
5.3.1	Ear Dipole Results	61
5.3.2	Cryo Kite Results	64
5.4	Summary	72
Chapter 6	Conclusion and Future Work	75
6.1	Future Work	75
REFERENCES	77

LIST OF TABLES

1.1	World-wide PAF research results to date	2
2.1	Parameters for the Ciao Wireless and Cryo-cooled LNAs.	15
2.2	Table of dipole designs.	19
3.1	Room temperature and cryo-cooled PAF design goals.	22
3.2	Room temperature and cryo-cooled PAF noise budget.	22
4.1	Model figures of merit for the single polarization Carter array.	33
4.2	Optimized parameters for the Carter array	35
4.3	Max sensitivity and minimum $T_{\text{sys}}/\eta_{\text{ap}}$ for the Carter array	46
4.4	Model and measured 20-Meter half-power beam width (HPBW) data for the bore-sight beam.	47
5.1	Maximum sensitivities for the dual pol ear array	64
5.2	Maximum sensitivities for the dual pol cryo kite array	72

LIST OF FIGURES

2.1	System diagram from arrays to beamformer.	8
2.2	Equivalent system with reference planes.	14
3.1	Single element model of thin dipole elements.	23
3.2	2008 Thin dipole array comparison plots	24
3.3	Original 50 Ω pictures	26
3.4	Original 50 Ω comparisons	27
4.1	Model representation of the ‘post’ design.	30
4.2	Model representation of the ‘kite’ design.	31
4.3	Model representation of the ‘Green Bank balun’ design.	31
4.4	Plots of model active impedances and sensitivity from the Carter array	34
4.5	Schematic drawing of the active impedance matched single pol element	35
4.6	Single isolated element impedance for modeled and built dipoles.	36
4.7	Single pol return and insertion loss plots	37
4.8	Return loss associated the center element of the nineteen element array.	38
4.9	Single pol system temperature and efficiency plots	39
4.10	Absorber platform construction pictures	40
4.11	Single channel equivalent noise temperatures.	41
4.12	The Arecibo radio telescope.	42
4.13	Arecibo’s overlapping array positions	43
4.14	Carter array super-fine sensitivity maps	44
4.15	Model and measured sensitivity and $T_{\text{sys}}/\eta_{\text{ap}}$ data plots.	46
4.16	Measured and model beam pattern cut comparisons.	48
5.1	Infinite array unit cell.	54
5.2	Top and side views of the spline, ear, and cryo kite dual pol element models.	58
5.3	Modeled sensitivity and active impedance plots for dual pol ear elements	59
5.4	Modeled sensitivity and active impedance plots for cryo kite elements	61
5.5	Dual polarization ear element sensitivity maps, single pol	63
5.6	Dual polarization ear element sensitivity maps with both polarizations	65
5.7	Model and measured sensitivity and $T_{\text{sys}}/\eta_{\text{ap}}$ plots for cryo kite elements.	67
5.8	Results from the hot-cold, Y-factor test performed on the cryo kite array	68
5.9	Cryo kite sensitivity maps, single pol	69
5.10	Cryo kite sensitivity maps with both polarizations	71

CHAPTER 1. INTRODUCTION

1.1 Radio Astronomy

Beginning with Karl Jansky's discoveries in the early 1930's [1], radio astronomy has transformed the way we look at the universe. Radio astronomy, referring to the use of non-optical frequencies for astronomical observation, provides avenues for technological development by requiring sophisticated, low-noise antennas and amplifiers as well as high quality filter designs to enable scientists to analyze and extract useful information from radio signals originating countless light-years away. This work focuses on the development of low-noise antenna arrays for use in radio astronomy.

1.2 Phased Arrays in Radio Astronomy

Although phased array feeds for communication systems have been in use for several years, they have only recently become accepted for use in the radio astronomy community. Historically, radio astronomers have utilized large single feeds or small arrays of elements with independent beams — such as the ALFA feed at the Arecibo Observatory [2] — which are not electrically steerable in the sense that we can combine the signals and steer the beam in any direction [3]. However, PAFs have the potential to provide several important benefits not available with previous feeds: PAFs can increase survey speed by providing steerable beams over a significant continuous field of view, increase sensitivity, and provide a means to mitigate radio frequency interference (RFI) [4], [5]. Millions of research dollars have already been spent in efforts to achieve these benefits.

Implementing phased arrays for radio astronomy, however, is not without its challenges. PAFs naturally have large mutual coupling due to there being many, closely spaced array elements, which can introduce impedance mismatches and signal loss. Channel gain stability, insufficient

Table 1.1: World-wide PAF research results to date.

Organization, Location	Element Type	Sensitivity	$T_{\text{sys}}/\eta_{\text{ap}}$
ASTRON, Netherlands [9]	Dual pol Vivaldi elements (2009)	5.5 m ² /K	89 K
CSIRO, Australia [10]	Dual pol patch elements (2010)	NA	175 K
BYU, USA	Single pol thin dipole elements (2008)	2.9 m ² /K	109 K

bandwidths, and developing RFI mitigation techniques sufficient for the low SNR environments typical in radio astronomy also complicate the work.

Presently there are several groups internationally working on PAFs for radio astronomy. In Canada, the Dominion Radio Astrophysical Observatory (DRAO) has been developing Vivaldi arrays for the Phased Array Feed Demonstrator system (PHAD) [6]. Similarly, a dual polarization, wideband Vivaldi array called APERTure Tile In Focus (APERTIF) is under development by The Netherlands Foundation for Research in Astronomy (ASTRON) [7]. Another group, the Australian Commonwealth Scientific and Industrial Research Organization (CSIRO) have been refining a square patch array, affectionately called the ‘checkerboard’ array, to be used on the Australian Square Kilometer Array Pathfinder (ASKAP) project [8]. Known array sensitivity and $T_{\text{sys}}/\eta_{\text{ap}}$ (see Section 2.3.5) measurements from these international organizations are presented in Table 1.1.

The Brigham Young University radio astronomy group has been working with the National Radio Astronomy Observatory (NRAO) to develop PAFs since 2005. Initial single polarization seven and nineteen element hexagonal array designs were built in 2006 and 2007 [11], [12], and tested on NRAO’s 20-Meter dish in Green Bank, West Virginia. Beginning in 2008, PAF design focus at BYU has shifted towards developing high-sensitivity, actively matched arrays that reduce array mutual coupling noise. After the successful implementation of an actively matched single polarization array in 2009, work on dual polarization arrays became a priority in early 2010 .

1.3 Thesis Contributions

Building on the work of [13], [14], [15], and [5], this thesis describes design processes and presents results for BYU radio astronomy PAF array designs as follows:

- Previous results are validated and new element designs, derived from thickened dipole concepts, are modeled using a finite element method (FEM) based commercial electromagnetic CAD software and software dish models.
- Both single and dual polarization room temperature dipole arrays as well as a liquid helium (cryo) cooled dual polarization array in hexagonal grids are optimized utilizing a low-noise active matching criterion.
- Measurements were taken in a variety of ways and places including at Brigham Young University on the Clyde building roof, on NRAO's 20-Meter dish in Green Bank, WV, and on the 300-meter dish at the Arecibo Observatory in Arecibo, PR. Model and measured results are compared in terms of system temperatures and sensitivity for available data sets.

The noise matching techniques described in this report are motivated by array mutual coupling effects discussed by [16], [17], [18], and [19]. As fully active impedance matched arrays for radio astronomy had never been realized, the goal of the presented research is to minimize mutual coupling noise for PAF systems by actively matching the array design impedance with our low noise amplifier's impedance. This process, if done correctly, results in an overall reduction in system noise temperature. The following chapters describe this work in detail.

1.4 Thesis Outline

This thesis is organized as follows:

Chapter 2, *Background*, describes the signal models assumed for on dish and hot-cold experiments and modeling. Array figures of merit and experimental techniques are derived and defined. Also, this chapter includes a table of element designs and their locations throughout the report.

Chapter 3, *Model Validation*, follows the work that was done to validate the 2008 thin dipole array and prepare for active matched array design. A 50 Ω dipole was designed, built, and measured scattering parameter values compared with model.

Chapter 4, *Single Polarization Feed Design*, describes the design and implementation of a single polarization nineteen element active impedance matched dipole array. Several initial ele-

ment designs were tested in software, before a final design was chosen and optimized in commercial electromagnetic design software. Experimental on dish results are given and explained.

Chapter 5, *Dual Polarization Feed Design*, details the development of several thirty-eight element dual polarization active impedance matched arrays. New array optimization methods are described and on dish results are provided for both room temperature and liquid helium cooled arrays.

Chapter 6, *Conclusion*, summarizes the contributions to the BYU radio astronomy group and the PAF community provided by this thesis. A short description of possible future work is also included.

CHAPTER 2. BACKGROUND

Building off of initial BYU radio astronomy system models, this chapter begins with a description of the signal model used to describe observations on dish. After a brief explanation of array beamformers and active impedances, array figures of merit are summarized and system receiver specifications are given. Finally, the hot-cold Y-factor technique is described with its corresponding noise terms and a table of pertinent antenna designs is presented.

2.1 Signal Model

The signal model assumes N elements pointed at a reflector dish, with voltage vector

$$\mathbf{v} = \begin{bmatrix} v_1 & v_2 & \cdots & v_N \end{bmatrix}^T.$$

These receiver output voltages are expressed in terms of signal and noise components

$$\mathbf{v} = \mathbf{v}_{\text{sig}} + \mathbf{v}_n, \quad (2.1)$$

where \mathbf{v}_{sig} is a vector of voltages associated with the signal of interest and \mathbf{v}_n is the voltages associated with noise. The noise consists of several contributors,

$$\mathbf{v}_n = \mathbf{v}_{\text{sp}} + \mathbf{v}_{\text{sky}} + \mathbf{v}_{\text{loss}} + \mathbf{v}_{\text{rec}}, \quad (2.2)$$

where \mathbf{v}_{sp} is the voltage due to spillover around the dish, \mathbf{v}_{sky} is the voltage attributed to thermal sky noise, \mathbf{v}_{loss} is the voltages from lossy/noisy elements, and \mathbf{v}_{rec} is the noise voltage associated with the receiver system [13]. In this case, \mathbf{v}_{rec} can be written as

$$\mathbf{v}_{\text{rec}} = \mathbf{v}_{\text{LNA}} + \mathbf{v}_{\text{rec2}},$$

where \mathbf{v}_{LNA} is the voltage due to amplifier noise and \mathbf{v}_{rec2} is the voltage due to the rest of the receiver chain (\mathbf{v}_{LNA} is much larger than \mathbf{v}_{rec2} and dominates \mathbf{v}_{rec}).

Spatially correlating these voltages and assuming that each component is independent of the others (i.e. $E[\mathbf{v}_{\text{sig}}\mathbf{v}_{\text{sky}}] = 0$) results in the following correlation matrices:

$$\begin{aligned}
\mathbf{R}_v &= E[\mathbf{v}\mathbf{v}^H] \\
&= E[\mathbf{v}_{\text{sig}}\mathbf{v}_{\text{sig}}^H] + E[\mathbf{v}_{\text{sky}}\mathbf{v}_{\text{sky}}^H] + E[\mathbf{v}_{\text{sp}}\mathbf{v}_{\text{sp}}^H] + E[\mathbf{v}_{\text{loss}}\mathbf{v}_{\text{loss}}^H] + E[\mathbf{v}_{\text{rec}}\mathbf{v}_{\text{rec}}^H] \\
&= \mathbf{R}_{\text{sig}} + \mathbf{R}_{\text{sky}} + \mathbf{R}_{\text{sp}} + \mathbf{R}_{\text{loss}} + \mathbf{R}_{\text{rec}} \\
&= \mathbf{R}_{\text{sig}} + \mathbf{R}_{\text{ext}} + \mathbf{R}_{\text{loss}} + \mathbf{R}_{\text{rec}} \\
&= \mathbf{R}_{\text{sig}} + \mathbf{R}_n,
\end{aligned} \tag{2.3}$$

where $E[\cdot]$ denotes expectation and \mathbf{R}_{ext} is the additive combination of \mathbf{R}_{sky} and \mathbf{R}_{sp} as external noise components (not associated with the array or receiver system). Matrix subscripts correspond to their voltage counterparts.

Oftentimes it is convenient to shift our reference point to immediately after the antennas and define a noise term associated with only non-receiver noise sources. Designated the array isotropic thermal noise correlation matrix, this noise term is defined

$$\mathbf{R}_t = \mathbf{R}_{\text{ext}} + \mathbf{R}_{\text{loss}},$$

where \mathbf{R}_{ext} is once again the combination of external noise components (\mathbf{R}_{sky} and \mathbf{R}_{sp}) and \mathbf{R}_{loss} is thermal noise due to loss in the feed. These matrices assume that the array and external environment are at a standard temperature. For model calculations this value, called the isotropic noise temperature T_{iso} , is assumed to be 290 K. However, since this temperature does not always hold for experimental observations, measurements are rescaled so that the equivalent T_{iso} equals 290 K.

Often it is convenient to model array systems with Thévenin equivalent networks that utilize open circuit voltages (\mathbf{v}_{oc}) for each incident field. Receiver output voltages relate to \mathbf{v}_{oc} through the linear transformation

$$\mathbf{v} = \mathbf{Q}\mathbf{v}_{\text{oc}}, \tag{2.4}$$

where the matrix \mathbf{Q} depends on receiver, LNA, and array network parameters [19].

2.1.1 Beamformers

Among the benefits of using PAFs in radio astronomy is the ability to utilize beamforming to broaden an array's field of view and increase survey speed. A signal processing technique that allows users to electrically steer an array in any direction, beamforming essentially creates a transmit or receive pattern that filters out undesirable signals. As the number of elements in the array increases, so does the number of available beams. Naturally, some formed beams are more useful than others.

Most optimizations and sensitivity comparisons in this report utilize a max-SNR beamformer [20]. The beam output SNR is

$$\text{SNR} = \frac{\mathbf{w}^H \mathbf{R}_{\text{sig}} \mathbf{w}}{\mathbf{w}^H \mathbf{R}_n \mathbf{w}}. \quad (2.5)$$

Maximizing with respect to \mathbf{w} requires a derivative that results in

$$\mathbf{R}_n^{-1} \mathbf{R}_{\text{sig}} \mathbf{w} = \left(\frac{\mathbf{w}^H \mathbf{R}_{\text{sig}} \mathbf{w}}{\mathbf{w}^H \mathbf{R}_n \mathbf{w}} \right) \mathbf{w}. \quad (2.6)$$

Taking this as an eigenvalue equation, the weight vector \mathbf{w} that maximizes SNR is then the eigenvector that corresponds to the largest eigenvalue.

For comparison, a center element beamformer is often used to turn off all but the center array element and is defined as

$$\mathbf{w}_c = \left[1 \ 0 \ 0 \ \dots \ 0 \right]^T. \quad (2.7)$$

Typically, beamformers are defined as coefficients applied to full-wave amplitudes at array input ports. Some applications, however, such as computing active impedances in commercial EM modeling codes, require the use of forward-wave amplitudes to produce beamformer outputs (\mathbf{w}_f). As the name implies, forward-wave beamformers are amplitudes of forward moving waves at array input ports.

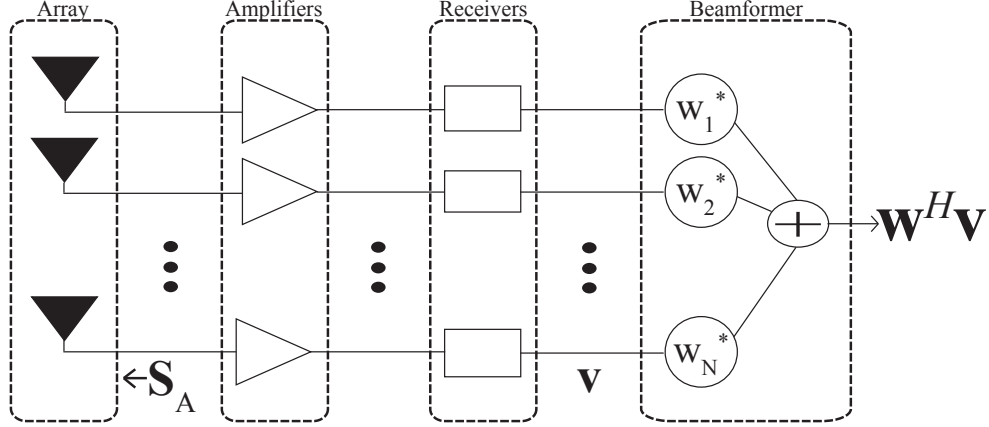


Figure 2.1: System diagram from arrays to beamformer.

2.2 Active Impedances

In order to reduce overall system noise, we seek to minimize noise from receiver components that contribute the bulk of the noise. Literature gives several ways to do this, among them: multiport decoupling networks, self-impedance matching, and active impedance matching.

Multiport decoupling networks, which diagonalize and uncouple the mutual impedance matrix, would by necessity be situated between the array and front end amplifier. Unfortunately, components placed before the low noise amplifier significantly increase system noise as their component noise is amplified along with the signal, which for astronomical observation is extremely small. Because of this noise amplification effect, multiport decoupling networks are particularly unsuited for use with phased arrays in radio astronomy.

Achieving self-impedance matches for phased arrays is simple and significantly reduces receiver noise, but is suboptimal in that it does not account for mutual coupling, array beamformer weighting, and signal processing. Although more complicated, active impedance matching compensates for beamformer weights and has the potential to achieve optimal noise reduction over a range of beam steering angles [19].

Active impedances are defined as

$$Z_{\text{act},m} = \frac{1}{w_{\text{oc},m}^*} \sum_{n=1}^N Z_{A,nm} w_{\text{oc},n}^* \quad (2.8)$$

where \mathbf{w}_{oc} is the open circuit beamforming coefficients and \mathbf{Z}_A is the original mutual impedance matrix. Utilizing a linear transform similar to Equation 2.4, \mathbf{w} can be found from \mathbf{w}_{oc} by

$$\mathbf{w} = (\mathbf{Q}^H)^{-1} \mathbf{w}_{oc}.$$

As can be seen from the above equations, active impedances are dependent on the applied beam and original mutual impedance matrix. Also of note are the active reflection coefficients

$$\Gamma_{act,m} = \frac{1}{w_{f,m}^*} \sum_{n=1}^N S_{A,nm} w_{f,n}^*, \quad (2.9)$$

where \mathbf{w}_f are forward-wave beamformers defined previously, and \mathbf{S}_A is the scattering matrix.

Physically, active impedances can be difficult to explain. In an ideal world, the array would be designed to eliminate mutual coupling altogether. As this is not possible, the goal of active impedance matching is to design the array in such a way that the magnitudes and phases of noise components due to mutual coupling cancel each other out as they are summed at the beamformer.

Referring Equation 2.9 to Figure 2.1, \mathbf{S}_A is the scattering matrix looking into the array element inputs. A signal sent into each element input will be reflected by some amount defined by the diagonal elements of the scattering matrix ($S_{A,nn}$). Some part of the signal will also couple between elements. For example, if a signal is input into element two, some portion of the signal will radiate from element two and be received by element one as noise. The amount of signal coupled in this way is represented by the off diagonal elements of the scattering matrix, in this case $S_{1,2}$. Each coupled noise term will have a magnitude and phase dependant on the scattering parameters (impedances) of the elements, which are in turn controlled by the element design. Since we are applying a known magnitude and phase weighting to the signal from each channel as it enters the beamformer, we can cancel out noise terms by designing the array such that these beamformer phases will sum noise contributions destructively. Active impedance matching, using the above equations, is a way to collectively sum a linear combination of signal and noise terms so that noise contributions add to zero by designing the array for specific impedances that take into account a desired beamformer.

2.3 Figures of Merit

The following definitions and derivations describe the most significant figures of merit for phased arrays in radio astronomy.

2.3.1 Radiation Efficiency

The beam radiation efficiency of a phased array is defined for a transmitter as

$$\eta_{\text{rad}} = \frac{P_{\text{rad}}}{P_{\text{in}}}, \quad (2.10)$$

where P_{rad} is power radiated and P_{in} is the total power input into the array. For receiving arrays, this equation changes to

$$\eta_{\text{rad}} = \frac{P_{\text{ext}}}{P_{\text{t}}} = \frac{P_{\text{ext}}}{P_{\text{ext}} + P_{\text{loss}}}, \quad (2.11)$$

where P_{ext} is the noise power associated with external noise, P_{t} is the noise power due to all noise terms before the receiver (including P_{ext}), and P_{loss} is the noise power due to antenna losses measured when the array and external environment are in thermal equilibrium at T_{iso} .

It should be noted that for convenience and efficiency in array modeling we often assume $\eta_{\text{rad}} \approx 1$. In reality, however, η_{rad} may be lower than unity depending on material choice and element design.

2.3.2 Aperture Efficiency

Aperture efficiency is the measure of how effectively a radiation pattern uses the physical area of a dish. Beginning with the IEEE standard definitions [21], we first define three antenna terms:

- Antenna efficiency for an aperture antenna is defined as

$$\eta_{\text{ant}} = \frac{A_{\text{e}}}{A_{\text{phy}}}, \quad (2.12)$$

where A_{phy} is the physical area of the aperture and A_{e} is the effective area.

- The effective area of an antenna is defined as the ratio of available power at the antenna terminals to the power flux density incident on the antenna, or

$$A_e = \frac{P_{\text{sig}}^{\text{av}}}{S^{\text{sig}}}. \quad (2.13)$$

With a little manipulation of Equation 2.13 [22], [23], A_e can be written

$$\begin{aligned} A_e &= \frac{\lambda^2}{4\pi} G_0 \\ &= \frac{\lambda^2}{4\pi} \eta_{\text{rad}} D_0, \end{aligned} \quad (2.14)$$

where λ is the signal wavelength, G_0 is the maximum antenna gain, and D_0 is the maximum antenna directivity.

- Aperture efficiency for an aperture antenna is defined as the ratio

$$\eta_{\text{ap}} = \frac{D_0}{D_{\text{std}}}, \quad (2.15)$$

where D_{std} is the antenna standard directivity. D_{std} is often written

$$D_{\text{std}} = \frac{\lambda^2}{4\pi} A_{\text{phy}}. \quad (2.16)$$

Combining Equations 2.14, 2.15, and 2.16, we arrive at the result:

$$\eta_{\text{ap}} = \frac{A_e}{\eta_{\text{rad}} A_{\text{phy}}}. \quad (2.17)$$

For our system it is most convenient to expand Equation 2.17 as per [24]

$$\eta_{\text{ap}} = \left(\frac{k_b T_{\text{iso}} B}{S^{\text{sig}} A_{\text{phy}}} \right) \left(\frac{\mathbf{w}^H \mathbf{R}_{\text{sig}} \mathbf{w}}{\mathbf{w}^H \mathbf{R}_{\text{iso}} \mathbf{w}} \right), \quad (2.18)$$

where k_b is Boltzmann's constant and B is the system bandwidth.

2.3.3 Spillover Efficiency

Similar to aperture efficiency, spillover efficiency characterizes how much of an array's pattern hits a reflector as opposed to 'spilling' over the sides. Since the ground is much warmer than the depths of space, seeing too much ground can destroy an array's sensitivity, making spillover a major contributor to the overall noise. From [25] it has been shown that spillover efficiency is

$$\eta_{\text{sp}} = 1 - \frac{T_{\text{iso}} \mathbf{w}^H \mathbf{R}_{\text{sp}} \mathbf{w}}{T_{\text{g}} \mathbf{w}^H \mathbf{R}_{\text{iso}} \mathbf{w}}, \quad (2.19)$$

where \mathbf{R}_{sp} is the correlation matrix corresponding to the voltages produced by spillover noise (part of \mathbf{R}_{iso}), and T_{g} is the temperature of the ground. This is sometimes written

$$\eta_{\text{sp}} = 1 - \frac{T_{\text{sp}}}{T_{\text{g}}}, \quad (2.20)$$

where T_{sp} is the equivalent spillover noise temperature.

2.3.4 System, Receiver, and LNA Noise Temperatures

Among the most telling figures of merit, system temperature T_{sys} describes the overall noise contribution of the system. From [26], T_{sys} is written as the ratio of beamformed noise contributions

$$\begin{aligned} T_{\text{sys}} &= T_{\text{iso}} \left(\frac{P_{\text{n}}}{P_{\text{t}}} \right) \\ &= T_{\text{iso}} \left(\frac{\mathbf{w}^H \mathbf{R}_{\text{n}} \mathbf{w}}{\mathbf{w}^H \mathbf{R}_{\text{t}} \mathbf{w}} \right). \end{aligned} \quad (2.21)$$

Similar to the correlation matrices described previously, T_{sys} can be broken down into its various components

$$T_{\text{sys}} = T_{\text{rec}} + T_{\text{sp}} + T_{\text{sky}} + T_{\text{loss}}, \quad (2.22)$$

where T_{rec} is the noise contribution of the receivers, T_{sp} is spillover noise, T_{sky} is the sky noise temperature (approximately 5 K at L-band), and T_{loss} represents ohmic losses in the antennas. Active impedance matching focuses on the largest of these components, T_{rec} .

It is known from basic noise-figure theory [27] that noise from cascaded systems increases as

$$T_{\text{cas}} = T_{e1} + \frac{T_{e2}}{G_1} + \frac{T_{e3}}{G_1 G_2} + \dots, \quad (2.23)$$

where T_{cas} is the overall noise temperature of the cascaded system, T_{e1} , T_{e2} , and T_{e3} are noise contributions from individual elements within the system, and G_1 and G_2 are element gains from the first two elements respectively. If these values are replaced by those from our receiver system, the resulting T_{rec} appears as

$$T_{\text{rec}} = T_{\text{LNA}} + \frac{T_{\text{rec2}}}{G_{\text{LNA}}} + \dots, \quad (2.24)$$

where T_{rec2} is the noise temperature of the down-converters and data acquisition system and G_{LNA} is LNA gain. Since the LNA gain is quite large at 40 dB (see Section 2.4 for more details), noise contributions from later receiver components are significantly reduced. As LNA noise dominates T_{rec} , we often approximate receiver noise as

$$T_{\text{rec}} \approx T_{\text{LNA}}. \quad (2.25)$$

T_{LNA} is then calculated by

$$T_{\text{LNA}} = T_{\text{iso}} \left(\frac{\mathbf{w}^H \mathbf{R}_{\text{LNA}} \mathbf{w}}{\mathbf{w}^H \mathbf{R}_t \mathbf{w}} \right), \quad (2.26)$$

where \mathbf{R}_{LNA} is assumed to be approximately equal to \mathbf{R}_{rec} .

We can also relate T_{LNA} to the LNA optimal reflection coefficient $\Gamma_{\text{LNA,opt}}$ and active antenna reflection coefficient Γ_{act} as follows:

$$T_{\text{LNA}} = T_{\text{min}} + \frac{4R_N T_0 |\Gamma_{\text{act}} - \Gamma_{\text{LNA,opt}}|^2}{Z_0 (1 - |\Gamma_{\text{act}}|^2) |1 + \Gamma_{\text{LNA,opt}}|^2}, \quad (2.27)$$

where R_N is the equivalent noise resistance of the amplifier, T_0 is the physical temperature of the transistor (assumed 290 K), and Z_0 is the characteristic impedances of the system (usually 50 Ω) [19].

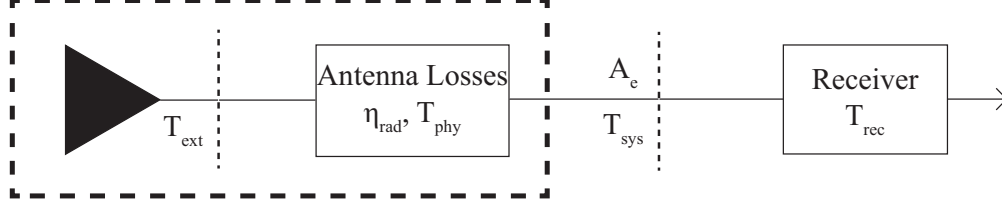


Figure 2.2: Equivalent system with reference planes.

2.3.5 Sensitivity

The ultimately desirable figure of merit for a phased array in radio astronomy, tying all others together, is sensitivity. Sensitivity is defined as

$$\begin{aligned}
 S &= \frac{A_e}{T_{\text{sys}}} & (2.28) \\
 &= \frac{\eta_{\text{rad}} \eta_{\text{ap}} A_{\text{phy}}}{T_{\text{sys}}} \\
 &= \frac{\eta_{\text{rad}} \eta_{\text{ap}} A_{\text{phy}}}{\eta_{\text{rad}} T_{\text{sp}} + \eta_{\text{rad}} T_{\text{sky}} + T_{\text{loss}} + T_{\text{rec}}} \\
 &= \frac{\eta_{\text{rad}} \eta_{\text{ap}} A_{\text{phy}}}{\eta_{\text{rad}} (1 - \eta_{\text{sp}}) T_{\text{g}} + \eta_{\text{rad}} T_{\text{sky}} + (1 - \eta_{\text{rad}}) T_{\text{phy}} + T_{\text{rec}}}, & (2.29)
 \end{aligned}$$

where η_{rad} is radiation efficiency. For our purposes A_e and T_{sys} are referenced between the antennas and receivers as per Figure 2.2. Because A_{phy} varies by dish, sensitivity is often normalized by A_{phy} and inverted into the useful quantity

$$\frac{A_{\text{phy}}}{S} = \frac{T_{\text{sys}}}{\eta_{\text{ap}} \eta_{\text{rad}}} \quad (2.30)$$

$$= \frac{T_{\text{sys}}}{\eta_{\text{ant}}}, \quad (2.31)$$

where $T_{\text{sys}}/\eta_{\text{ant}}$ is in Kelvin. However, since η_{rad} is frequently assumed to be near unity it is often ignored, reducing $T_{\text{sys}}/\eta_{\text{ant}}$ to $T_{\text{sys}}/\eta_{\text{ap}}$.

Table 2.1: Parameters for the Ciao Wireless and Cryo-cooled LNAs.

LNA Parameters (1.6 GHz)	Ciao Wireless LNA	Cryo-cooled LNA
T_{\min}	33.15 K	6.29 K
\mathbf{Z}_{opt}	$49.45 + j7.26 \Omega$	$71.2 + j15.7 \Omega$
R_N	3.40 Ω	0.706 Ω
Gain	40 dB	39.2 dB

2.4 BYU Radio Astronomy Receiver Specifications

As receiver noise is the major contributor to overall system noise temperature, measures were taken to reduce individual component noise in the receiver chain. As discussed in Section 2.3.4, noise reduction is particularly important for the low noise amplifier stage immediately following the feed as any noise added will be continually amplified throughout the system. To this end, room temperature Mini-Circuits (ZEL-1217 LN) LNAs with $T_{\text{LNA},\min} \approx 120\text{K}$ and 29 dB of gain used in early experiments with the thin dipole array were replaced by Ciao Wireless LNAs with $T_{\text{LNA},\min} \approx 33\text{K}$ and 40 dB of gain in 2008. Also, in mid 2011 several experiments were performed with liquid-helium cooled (cryo-cooled) CITLF4 LNAs which have a $T_{\text{LNA},\min}$ of approximately 6.29 K at 1.6 GHz.

Because LNA gain is quite large with the Ciao Wireless LNA's, down-converter contribution is less significant to the overall receiver temperature as per Equation 2.24. However, improvement was still made from the connectorized component receiver box ($T_{\text{rec}2} \approx 1810\text{K}$) to Vikas Asthana's receiver cards ($T_{\text{rec}2} \approx 1622\text{K}$).

2.5 Hot-Cold Y-factor Technique

Without a dish nearby to make full system observations, we can still make several helpful measurements through hot-cold Y-factor noise techniques. These methods require the measurement of array outputs in two difference isotropic thermal environments — each with their own temperatures — allowing for the calculation of the isotropic noise environment and receiver correlation matrices \mathbf{R}_{iso} and \mathbf{R}_{rec} . Although the details are given more fully in [26], the following

equations and brief explanations provide the necessary background for the work detailed later in Sections 4.4 and 5.3.2.

The most convenient way to measure known temperatures would be to use ideal black bodies. However, as ideal black bodies are unavailable, hot-cold measurements are obtained through the following two array pointings:

1. Pointing the array towards the cold depths of space and taking data.
2. Covering the array with RF absorber and again taking data.

It is assumed that the sky has a temperature of 5 K with an additional 1.7 K from scattering along the horizon [28], whereas RF absorber is roughly the physical temperature of the surrounding environment. Conforming with previous notation these temperatures will be labeled T_{cold} and T_{hot} respectively.

As the signal model described in Section 2.1 applies only to on dish situations, a separate signal model is required for hot-cold measurements. Assuming that a perfect ground shield is used (blocking all ground noise), voltages at the receiver are defined in two ways:

$$\mathbf{v}_{\text{hot}} = \mathbf{v}_{\text{hot,ext}} + \mathbf{v}_{\text{rec}} \quad (2.32)$$

and

$$\mathbf{v}_{\text{cold}} = \mathbf{v}_{\text{cold,ext}} + \mathbf{v}_{\text{rec}}, \quad (2.33)$$

where $\mathbf{v}_{\text{hot,ext}}$ and $\mathbf{v}_{\text{cold,ext}}$ are voltages associated with observing RF absorber and the sky respectively. Because one of the objectives of the hot-cold analysis is a close approximation of \mathbf{R}_{iso} , both $\mathbf{v}_{\text{hot,ext}}$ and $\mathbf{v}_{\text{cold,ext}}$ measurements are made under the assumption that the array is in an isotropic noise environment. Taking the expected value with this assumption leads to

$$E [\mathbf{v}_{\text{hot}} \mathbf{v}_{\text{hot}}^H] = \frac{T_{\text{hot}}}{T_{\text{iso}}} \mathbf{R}_{\text{iso}}.$$

Since \mathbf{v}_{hot} and \mathbf{v}_{cold} are uncorrelated with \mathbf{v}_{rec} , we can define the following correlation matrices:

$$\mathbf{R}_{\text{hot}} = \frac{T_{\text{hot}}}{T_{\text{iso}}}\mathbf{R}_{\text{iso}} + \mathbf{R}_{\text{loss}} + \mathbf{R}_{\text{rec}} \quad (2.34)$$

$$\begin{aligned} &= \frac{T_{\text{hot}}}{T_{\text{iso}}}\mathbf{R}_{\text{iso}} + \mathbf{R}'_{\text{rec}} \\ &= \frac{\mathbf{R}_{\text{iso}}}{T_{\text{iso}}} + \frac{\mathbf{R}'_{\text{rec}}}{T_{\text{hot}}}, \end{aligned} \quad (2.35)$$

where $\mathbf{R}'_{\text{rec}} = \mathbf{R}_{\text{rec}} + \mathbf{R}_{\text{loss}}$. Likewise we define

$$\begin{aligned} \mathbf{R}_{\text{cold}} &= \frac{T_{\text{cold}}}{T_{\text{iso}}}\mathbf{R}_{\text{iso}} + \mathbf{R}'_{\text{rec}} \\ &= \frac{\mathbf{R}_{\text{iso}}}{T_{\text{iso}}} + \frac{\mathbf{R}'_{\text{rec}}}{T_{\text{cold}}}. \end{aligned} \quad (2.36)$$

Solving for \mathbf{R}'_{rec} by subtracting Equations 2.35 and 2.36 results in the equation

$$\mathbf{R}'_{\text{rec}} = \frac{\mathbf{R}_{\text{cold}}T_{\text{hot}} - \mathbf{R}_{\text{hot}}T_{\text{cold}}}{T_{\text{hot}} - T_{\text{cold}}}. \quad (2.37)$$

Substituting Equation 2.37 back into either Equations 2.35 or 2.36 and solving for \mathbf{R}_{iso} reduces to

$$\mathbf{R}_{\text{iso}} = \frac{T_{\text{iso}}}{T_{\text{hot}} - T_{\text{cold}}} (\mathbf{R}_{\text{hot}} - \mathbf{R}_{\text{cold}}). \quad (2.38)$$

Assuming system channel gains are stable and known when taking these measurements, we can approximate on dish T_{LNA} and T_{rec} for any known beam using Equation 2.26. If this assumption does not hold, channel gain variations cannot be compensated for and calculating T_{LNA} is not possible for arbitrary beams. Fortunately, single channel equivalent temperatures can be calculated regardless of channel gains.

2.5.1 Single Channel Equivalent Temperatures

As mentioned above, calculating receiver temperatures for arbitrary beams cannot be done without known, stable channel gains. The reason for this is that in order to correctly calculate beamformer magnitudes that are tuned to a particular beam, we must already know how much

the system is preamplifying each channel. Unstable channel gains are particularly difficult since channel gains can change over time, making system calibration that much more difficult. Unfortunately, neither the receiver system or post-processing algorithms can compensate for unknown or varying channel gains. However, useful information can still be gleaned from individual channel data. This can be done in two equivalent, but enlightening ways:

1. Defining the single channel Y-factor as

$$Y_i = \frac{[\mathbf{R}_{\text{hot}}]_{ii}}{[\mathbf{R}_{\text{cold}}]_{ii}}, \quad (2.39)$$

single channel equivalent temperatures can be expressed

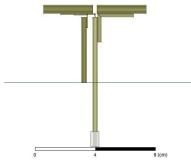
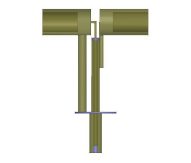
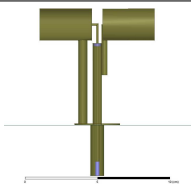

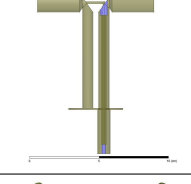
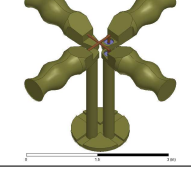
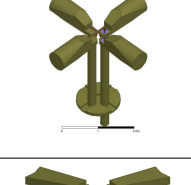
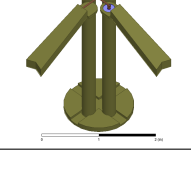
$$T_{\text{eq},i} = \frac{T_{\text{hot}} - Y_i T_{\text{cold}}}{Y_i - 1}. \quad (2.40)$$

2. Utilizing Equation 2.26 and employing a beamformer with only one nonzero coefficient (set to unity) similar to the center element beamformer of Equation 2.7, the resulting T_{LNA} can be shown to be equivalent to T_{eq} .

2.6 Table of Antennas

This section is to provide a reference table of modeled and constructed array elements.

Table 2.2: Table of dipole designs.

Model Name	Thumbnail	Status	Location in Thesis
2008 Thin Dipole		Constructed and used (2008)	Section 3.2
Original 50 Ω Dipole		Constructed and used (2009)	Section 3.3
Post Dipole		Model only (2009)	Section 4.1.1
Kite Dipole		Model only (2009)	Section 4.1.2
2009 Green Bank Balun Dipole		Constructed and used (2009)	Section 4.1.3
Spline Dipole		Model only (2010)	Section 5.2.1
2010 Ear Dipole		Constructed and used (2010)	Section 5.2.2
2011 Cryogenic Kite Dipole		Constructed and used (2011)	Section 5.2.3

CHAPTER 3. MODEL VALIDATION

Before designing new nineteen element arrays it was judged necessary to prove the accuracy of results from our computational electromagnetics software using previous designs and new, lower-loss single element models as benchmarks. As some components of previous BYU radio astronomy arrays were not fully modeled, this process began by completely modeling the 2008 thin dipole array developed by David Jones [13], James Nagel [15], and Jacob Waldron [14] for comparison with previously measured results. The following sections illustrate how array model comparisons were made and describes the modeling work required to validate results.

3.1 PAF Design Goals

Because the new generation of PAFs for radio astronomy require significant improvements in performance over the thin dipole array described in Section 3.2, several figure of merit design goals were determined for both room temperature and cryo-cooled arrays as per Table 3.1¹. Similarly, Table 3.2 depicts the noise budget assumed to reach T_{sys} and sensitivity goals where T_{loss} is an approximate ohmic loss value and T_{sp} is calculated using the design goal η_{sp} and a T_{g} of 290 K (see Equation 2.20). The sequence of array designs described in this thesis represents a research path towards a feed that meets all of these goals for both room temperature and cryo-cooled arrays.

3.2 Thin Dipole Array

The BYU Radio Astronomy group's previous work with phased arrays was limited to self-impedance matched seven and nineteen element arrays. These arrays, dubbed the thin dipole arrays due to their construction, performed well but with high overall T_{sys} . In moving to the next generation design it was deemed important to prove that our software models could provide accurate results for phased arrays. Previous modeling, which omitted baluns and used lumped

¹Sensitivity goal values assume a dish with twenty meter diameter, or an A_{phy} of 100π square feet.

Table 3.1: Room temperature and cryo-cooled PAF design goals.

Parameter	Room Temp. Value	Cryo-Cooled Value
Center Frequency	1.6 GHz	1.6 GHz
Bandwidth	≥ 300 MHz	≥ 300 MHz
Aperture Efficiency, η_{ap}	$\geq 70\%$	$\geq 70\%$
Spillover Efficiency, η_{sp}	$\geq 98\%$	$\geq 98\%$
Radiation Efficiency, η_{rad}	$\geq 98\%$	$\geq 98\%$
System Temperature, T_{sys}	≤ 51 K	≤ 24 K
Sensitivity	≥ 4.3 m ² /K	≥ 9.1 m ² /K

Table 3.2: Room temperature and cryo-cooled PAF noise budget.

Noise Term	Room Temp. Value	Cryo-Cooled Value
LNA Noise, T_{LNA}	37 K	10 K
Sky Temperature, T_{sky}	5.0 K	5.0 K
Ohmic Losses, T_{loss}	4.0 K	4.0 K
Spillover Temperature, T_{sp}	5.0 K	5.0 K
System Temperature, T_{sys}	51 K	24 K

element sources, sufficed for the original arrays as high sensitivity was not their objective and some loss was acceptable. However, more precise models were necessary to improve impedance matching for future designs.

In creating a faithful representation of the thin dipole array, the new software model included dimensions measured from the thin dipole array, full length quarter-wave baluns, and utilized wave-port sources (Figure 3.1). These changes reference scattering parameters to the low-noise amplifier (LNA) connection rather than at the feed and made for more accurate field models. For comparison, full nineteen element thin dipole array scattering parameters were measured on a network analyzer (measured four ports at a time with 50 Ω loads on all unconnected ports). As seen in Figure 3.2(a), modeled S-parameters for the center element match well for lower frequencies with the measured data. Higher frequency model results, however, deviate from measured data, particularly at the center frequency (1.6 GHz). These discrepancies are likely due to slight physical differences between actual dipoles and model dipoles that inductively change the array's impedance more at higher frequencies.

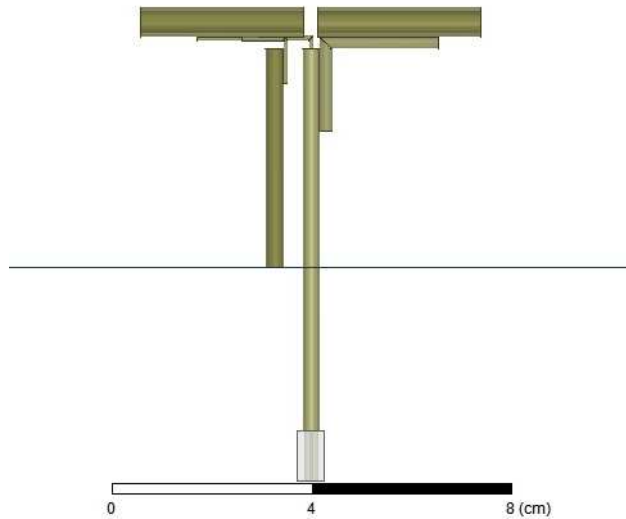


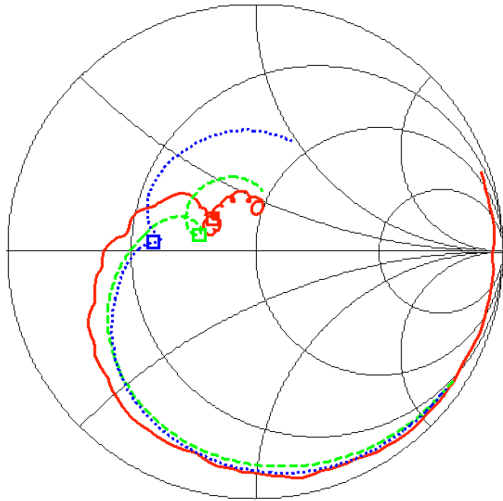
Figure 3.1: Single element model of thin dipole elements.

Data taken on the 20-Meter dish in Green Bank, WV in August 2008 provide the elevation and cross-elevation sensitivity cuts as seen in Figures 3.2(c) and 3.2(d). Both measured cuts, derived from the sensitivity map of Figure 3.2(b), match the shape of model cuts, but have lower sensitivity and are slightly wider. Measured sensitivity is generally about 15% lower than expected, probably due to dipole losses from poor construction. Although the model matches well overall, sensitivity and T_{sys} error are too large to neglect in future feed designs.

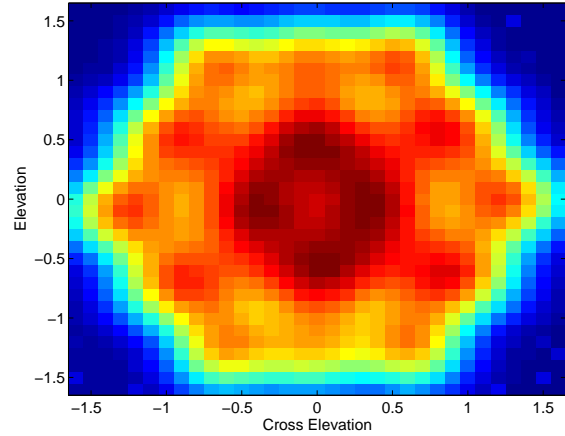
3.3 Single Element 50 Ω Match

As designing low-noise, high-sensitivity phased arrays was the ultimate goal, three significant design issues needed to be confronted:

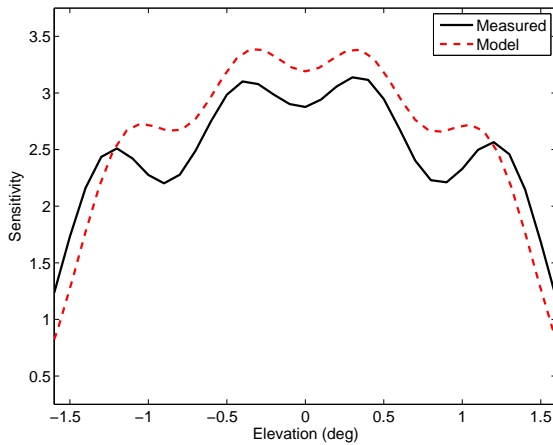
- Ohmic losses from poor construction and material choice add noise and reduce array sensitivity.
- Because elements need to be structurally sturdy, outdoor ready (weather proof), maintain their RF attributes, and be relatively inexpensive, manufacturability was a big concern.
- Thin dipoles are narrow-band by nature, so finding ways to get a good impedance match over larger bandwidths (300-500 MHz bandwidth at 1.6 GHz) was a priority.



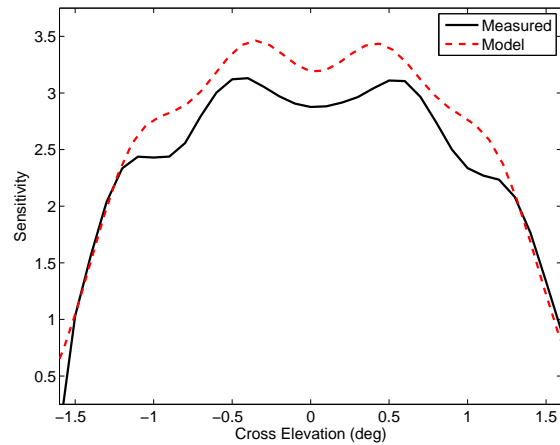
(a) Center element impedances for the thin dipole array. The solid line is measured, dashed modeled HFSS, and dotted modeled CST.



(b) Measured sensitivity map.



(c) Elevation sensitivity cuts.



(d) Cross elevation sensitivity cuts.

Figure 3.2: Model and network analyzer measured impedance comparisons as well as August 2008 on dish experimental data sensitivity calculations (max-SNR beamformer recomputed at each angle). For more details on Figures 3.2(b), 3.2(c), and 3.2(d) see [29].

These issues were met in several ways. To overcome ohmic losses, multiple adjustments were made in each dipole design. For example, where the thin dipole array used Teflon filled coax, new models reduced loss by implementing air filled coax. Although designing $50\ \Omega$ air filled coax is theoretically simple, the challenge is in finding ways to support the coax center (preventing it from touching surrounding walls) without making it expensive to manufacture. The final coax design utilized two Teflon beads, one at either end of the line, to center the inner conductor and transition to SMA connectors. Ohmic losses were reduced further by thickening elements components, allowing currents to spread across a larger surface area. This feature also increased antenna bandwidth as thickening dipole arms allows impedance matches over larger portions of the band. Finally, in an effort to validate our mechanical model and determine a fabrication process, three manufacturing engineering students and several precision machine laboratory (PML) technicians were consulted at various stages throughout the array design process.

In order to incorporate these element adjustments and mechanical processes as well as to determine an appropriate element starting structure for array design, a single dipole element was designed, optimized in software to a $50\ \Omega$ match, and built to specifications. Conveniently, this choice also produced a 50 ohm matched dipole for other uses.

Utilizing a basic dipole structure and including an in-model ground plane, this first $50\ \Omega$ matched design implements a system of quarter-wave balun posts and coax tubes to support the dipole arms (see Figure 3.3(a)). As mentioned, air-filled coax with two Teflon beads at either end was used. Finally, a copper disk was inserted at the base of the balun that screws down through the ground plane so that the dipole could be removed without desoldering.

Taking advantage of a quasi-Newton algorithm within the software modeler (HFSS Optimetrics) to minimize the magnitude of the reflection coefficient ($|S_{11}|$) at 1.6 GHz, I allowed the arm radius, arm height, and feed gap to vary. Figure 3.3(b) shows the completed dipole as constructed by the BYU PML. Made of copper with silver solder joints, the final dipole was slightly shorter than the model because of some difficulties in drilling out the coax and includes a screw on extension that lies below the ground plane so as not to influence the dipole's field response. As we typically connect our phased arrays with SMA cable, the end of the coax was fitted with a commercial male SMA connector using retaining rings (bottom of Figure 3.3(b)).

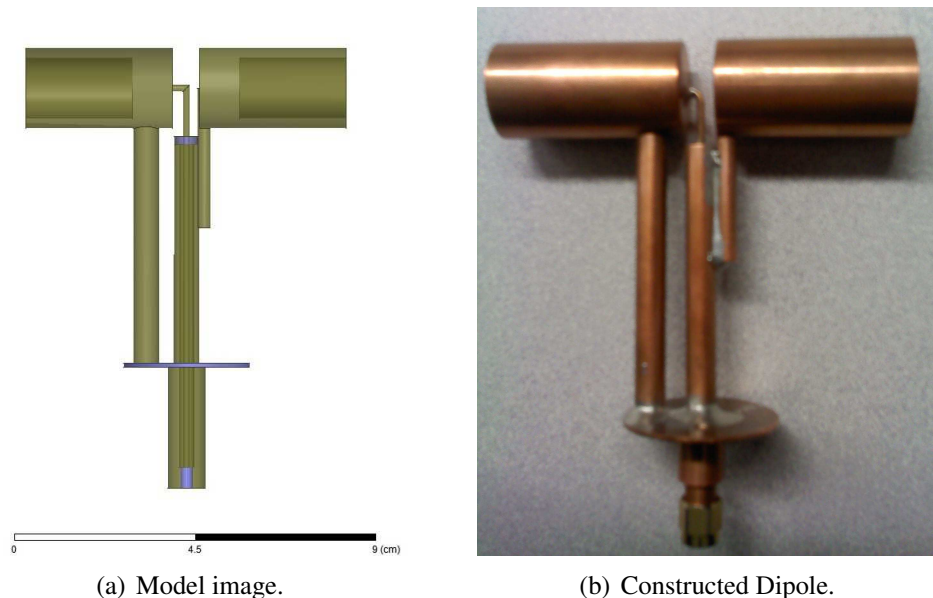


Figure 3.3: This figure shows pictures of the model and corresponding constructed antenna for the original 50 ohm matched dipole.

As per Figure 3.4, model and measured results can be shown to match reasonably well. However, measuring the scattering parameters using a network analyzer required the use of a SMA to N-type Teflon filled adapter, adding approximately 2 cm of reference shift ($\epsilon_r = 2.1$). To correct for this shift, a reverse 2 cm shift was applied in Matlab processing. Variations in actual adapter length and losses inherent to using additional connectors likely attributed to measured discrepancies.

It is instructive to scrutinize both the Smith chart and return loss plots (Figures 3.4(a) and 3.4(b)). In the Smith chart it can be seen how closely the shapes match over frequency, with the measured line shifted slightly downward. The model curve includes a loop around the center of the Smith chart, indicating a section of good bandwidth corresponding to a noticeably high section on the return loss plot. Measured results show a similar loop, but one that has been shifted off the center of the Smith chart. The downward shift of the model implies a capacitive impedance somewhere in the system that was not accounted for in the model.

The return-loss plot provides an overall indicator of how well the systems match to 50 ohms. A downward shift in the measured system's impedances on a Smith chart results in a lower return-loss peak around the center frequency (1.6 GHz) and an extra peak at 1.8 GHz. However,

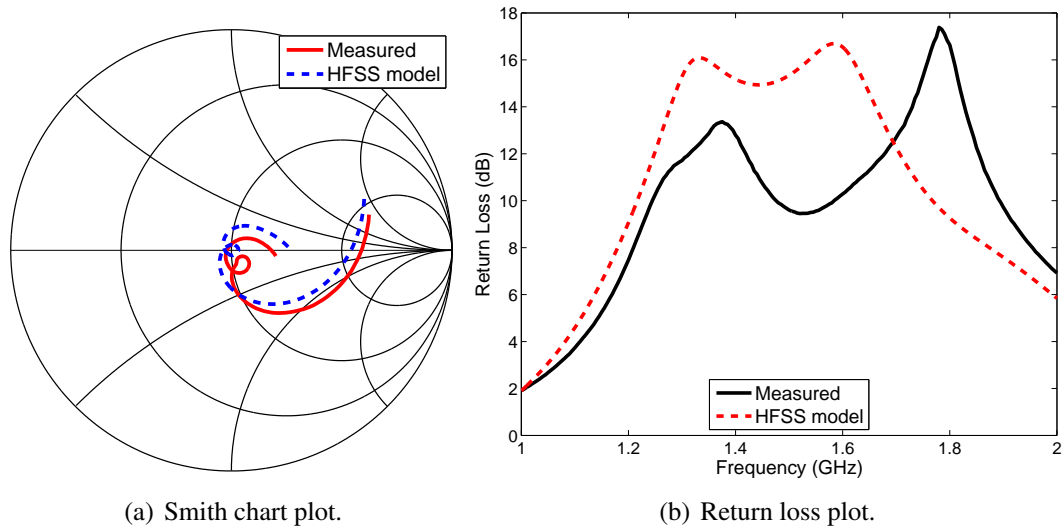


Figure 3.4: Single element 50 Ω match comparison of built and computer model.

because the overall shape remains quite similar (mostly a difference in return loss magnitude), we felt this validated the overall design procedure and provided a means to move on to full phased array systems.

3.4 Summary

This chapter has described steps taken to verify model reliability. The 2008 thin dipole array was completely remodeled and resulting scattering parameters and sensitivities compared with measured results; scattering parameters matched well, though higher frequencies were less accurate, and measured sensitivities were on average about 15% lower than expected. Also, a 50 Ω dipole was designed using new lower-loss components and techniques. As the 50 Ω dipole was well matched and legitimized our new modeling and manufacturing strategy, we then transitioned to full array design.

CHAPTER 4. SINGLE POLARIZATION ARRAY FEED DESIGN

Having verified that our electromagnetic design software can effectively model and optimize an antenna for a scattering parameter match, the next challenge was in moving to full phased array designs with active-impedance matching. This chapter describes the design and optimization of the original Carter array: a nineteen element active-matched phased array feed (PAF). As commercial EM software was unable to make all the necessary optimization cost function calculations internally, special techniques were designed and applied in conjunction with array optimization to allow for use within HFSS's Optimetrics application.

4.1 Single Polarization Phased Array Feed

In an effort to test various dipole-based element shapes and support structures, three variations of single polarization phased arrays were modeled and optimized (which process will be described shortly). These models are the 'post', 'kite', and 'Green Bank balun' designs.

4.1.1 The 'Post' Design

The first design, the post, comes directly from the 50Ω matched antenna described previously (Chapter 3). As shown in Figure 4.1, the post design utilizes a cylindrical dipole with a quarter wave balun supporting one arm while the other arm is supported by a post that connects to and derives its strength from the center coax. One significant disadvantage of the post is that the feed point separation (distance between antenna arms) is actually limited by the post, reducing its optimizable space.

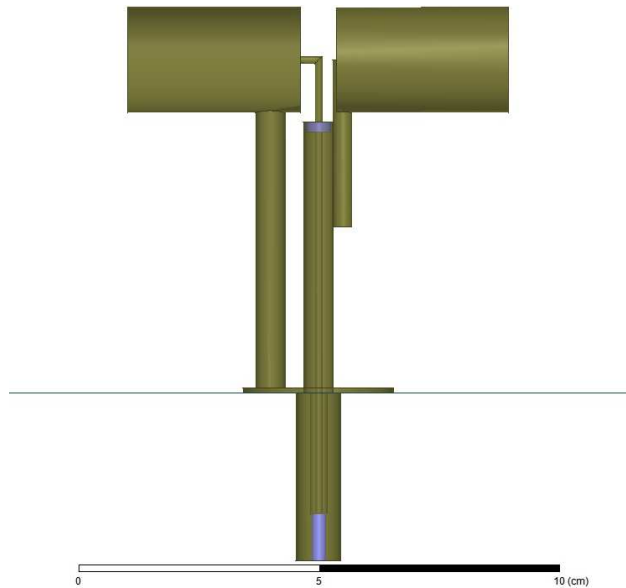


Figure 4.1: Model representation of the ‘post’ design.

4.1.2 The ‘Kite’ Design

The kite model uses a support structure similar to the post, but the arms were designed as flat ‘kite’ shaped pieces (see Figure 4.2). One advantage the kite has over the other models is that its shape provides more optimizable parameters (i.e., each corner of the kite can be placed independently). While the kite’s impedance matching and efficiency characteristics proved insufficient to make it the best choice for a single pol design, its shape influenced later dual pol models.

4.1.3 The Green Bank Balun Design

Finally, the Green Bank balun model is the third (and best) single pol design. The name ‘Green Bank balun’ relates to its originators in Green Bank, WV (NRAO) who provided us with the unoptimized dipole design. As per Figure 4.3, the antenna uses cylindrical arms that taper to where they connect with both the quarter-wave balun and coax. Unfortunately this connection proved a weakness in the structural design as the arms occasionally broke off constructed dipoles because of poor solder joints. However, the taper helped provide larger bandwidths and was therefore left in the design.



Figure 4.2: Model representation of the ‘kite’ design.

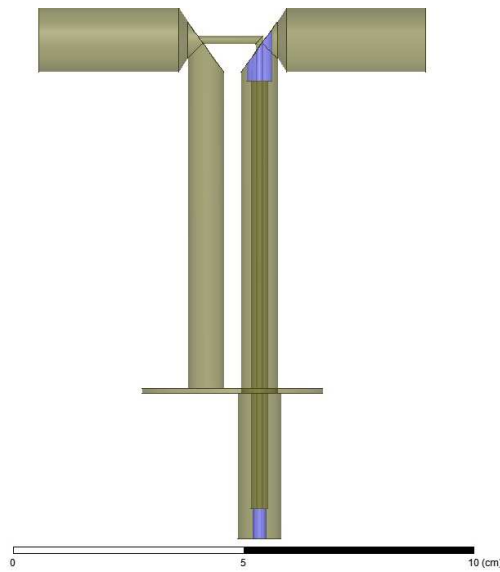


Figure 4.3: Model representation of the ‘Green Bank balun’ design.

4.2 Active Impedance Matched Array Design Technique

Starting with the three basic dipole designs outlined above, I utilized the built-in optimization function within our EM software (HFSS’s Optimetrics) to active impedance match nineteen element phased arrays. Each array was organized in a hexagonal grid with 0.6λ spacing between adjacent elements. Because the Green Bank balun dipole array performed the best in modeling,

survived the full optimization process, and was the only system built, the following section will focus on the procedure used for its analysis.

Using a Quasi-Newton optimization technique, a single element dipole on ground-plane was first optimized to a 50Ω self-impedance match at 1.6 GHz. To find the best match within the design space, the following design variables were allowed to vary: arm length, arm radius, arm height above the ground-plane, and separation between dipole arms (feed gap). Table 4.2 shows the final optimized dimensions for the isolated dipole. With this matched single element as a starting point for array optimization, a seven element hexagonal, single polarization phased array was then created. Again in software, the seven element array was itself optimized for a 50Ω self-impedance match to create an array that could be most efficiently optimized for active impedances.

Because impedance matching and array design take time, we opted to keep as much of the data processing within our EM software as possible. However, since active impedance calculations within HFSS require forward-wave beamforming coefficients, it was necessary to export fields and mutual impedances into MATLAB (MathWorks, Inc., Natick, MA) so as to provide some initial conditions. Utilizing system level modeling codes written by Karl Warnick, David Jones [13], and Jonathan Landon, with contributions from Mike Elmer, Taylor Webb, and David Carter to read in and incorporate the exported files and account for reflector optics, the noise response could then be calculated for spillover, ohmic loss, impedance mismatches at the LNA, and the sky. Max-SNR forward-wave beamforming coefficients were then determined as per the equations of Section 2.1.1 and input back into our commercial EM software. Incidentally, since beamformers were only calculated once (at the beginning of each optimization), this approach tended to work poorly as design parameters moved further from initial values; as the array morphed so did its fields, meaning that the original beamformers did not necessarily correspond to a max-SNR beam for the latest iteration. However, it was assumed that an appropriate array could be found in our design space wherein the actual max-SNR beamformers would be close enough to the optimizer's to provide a sufficient match. Stated another way, we believed that the optimizer could find an optimal match despite varying from the original beamformers because as we narrowed in on the optimal array the fields would change less and less. Therefore, because the beamformer coefficients were updated periodically and the array was changing less, we assumed that the final array would provide active impedances matched to the correct, or at least a very similar, beam.

Table 4.1: Model figures of merit for the single polarization Carter array.

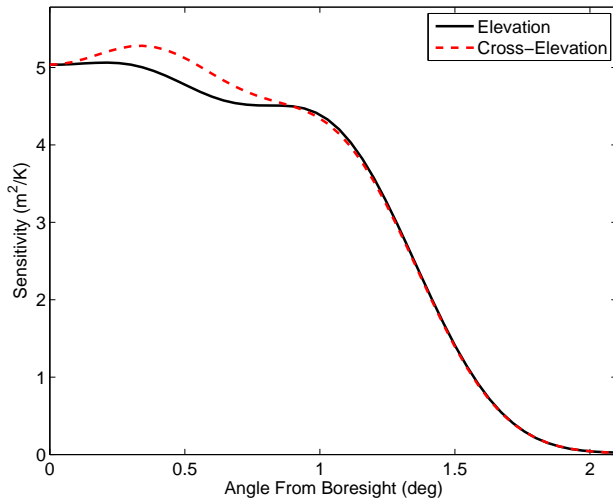
Parameter	Value
η_{ap}	65.8%
η_{sp}	99.1%
T_{loss}	2 K
T_{sky}	5 K
T_{LNA}	35.5 K
T_{sys}	50.1 K
$T_{\text{sys}}/\eta_{\text{ap}}$	76.1 K
Sensitivity	4.13 m ² /K

With model beamforming coefficients defined within the optimization software, another Quasi-Newton method was applied to the seven element array. This time, however, the algorithm was directed to optimize over active reflection coefficients. Because the center element contributes the largest noise temperature for a boresight steered max-SNR beam (the center element has the largest beamformer weight), the cost function was constrained so that the relative weights of the center element match to outer element match was five to one. While other weighting ratios were also tried (i.e. ten to one, one to one, etc...), a five to one ratio resulted in the best active matched array. Upon completion of seven element simulations, the array was scaled up to nineteen elements and again optimized for active impedances with a five to one matching constraint, ultimately producing the sensitivity curve seen in Figure 4.4(a). Figure 4.4(b) shows the array element active impedances for the model max-SNR beam at 1.6 GHz on a Smith chart as well as their proximity to the optimal LNA impedance. Of particular importance, the center element impedance lies almost on top of $\Gamma_{\text{LNA,opt}}$. Other model figures of merit are listed in Table 4.1.

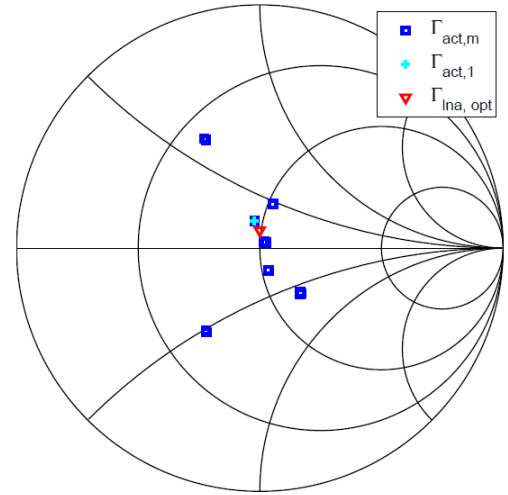
The final, fully constructed and active matched Carter array is shown in Figure 4.4(c). Each element in the array was assembled to the specifications displayed in Figure 4.5, where parameters one through five (P1 through P5) are the optimized dimensions described previously and defined in Table 4.2.

4.3 Modeled and Measured Return Loss

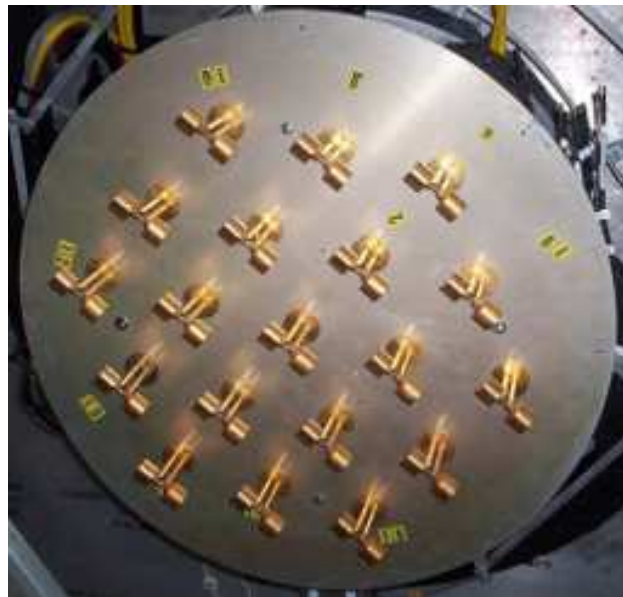
In order to characterize array elements and determine machinability a single dipole element was built to the optimized specifications obtained from software and its impedance measured with



(a) Optimal active impedance matched sensitivity vs. angle at 1.6 GHz.



(b) Element by element active impedances on a Smith chart for the max-SNR beam. An optimal match would mean that all the element $\Gamma_{act,m}$ were on top of $\Gamma_{LNA,opt}$.



(c) Picture of the full Carter array.

Figure 4.4: Plots of model active impedances and sensitivity from the Carter array at 1.6 GHz and a picture of the Carter array as mounted on the platform in Arecibo, PR. Sensitivity values shown are optimal in the sense that no ohmic losses or spillover due to scattering were accounted for and the assumed T_{sky} is only 3 K.

Table 4.2: Optimized parameters for the Carter array. Each dimension shown in mm.

Parameter	Isolated Dipole	Active Impedance Matched Element
Arm Length (P1)	29.00	29.08
Arm Taper Length (P2)	1.30	1.73
Post Separation (P3)	5.76	2.54
Dipole Radius (P4)	7.63	11.06
Dipole Height (P5)	69.37	59.40

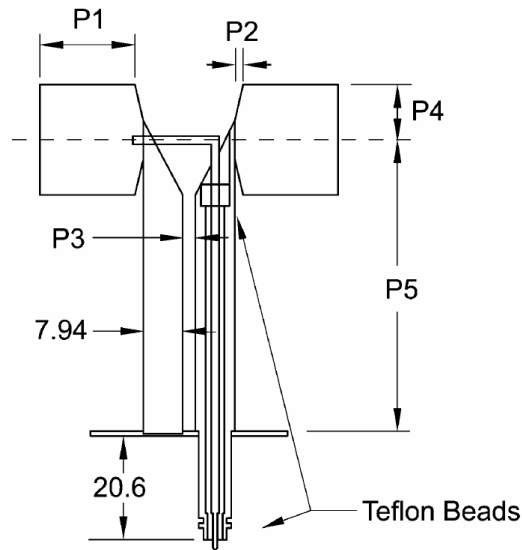


Figure 4.5: Schematic drawing of the active impedance matched single pole element for the Carter array. Dimensions are in mm.

a network analyzer. For comparison, a single element model with ground-plane was modeled and simulated over 1-2 GHz and scattering parameters in return-loss form can be seen contrasted with measured values in Figure 4.6. With model and measured isolated scattering parameters matching well over the bandwidth the other eighteen elements were built.

A four port network analyzer was again utilized to determine embedded array impedances for the full nineteen element array. Measurements were made with all unconnected ports loaded with 50Ω and resulting return-losses are compared with modeled results for the center element and elements of each ring of the hexagon in figures 4.7(a), 4.7(b), and 4.7(c). Each plot also contains active impedance match lines, where active impedances are calculated from model/measured self-impedances and model fields (actual array fields have not been measured). For completeness,

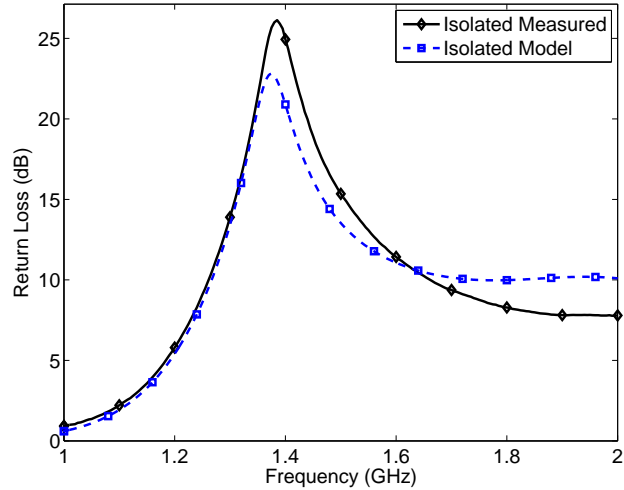


Figure 4.6: Single isolated element impedance for modeled and built dipoles.

Figures 4.7(d) and 4.7(e) show insertion loss for several similar elements. Fortunately, all figures display strong similarities between model and measured results, suggesting that our model is realistic.

Figure 4.8 provides a side-by-side summary comparison of the isolated element return-loss (see Figure 4.6), the embedded element return-loss, and the active matching return-loss (see Figure 4.7(a)) for the center element. As shown, the active match return-loss frequency shifts the match from 1.4 GHz to 1.6 GHz; while optimizing we found that the best active matched array at 1.6 GHz had a self-impedance match at 1.4 GHz. Again, these active impedance estimates were calculated using impedances measured on the network analyzer along with fields from the model since BYU’s location does not permit the on dish experimentation required to calculate array beamformer weights needed for an actual active impedance comparison. As a second check on receiver and LNA noise, hot-cold Y-factor measurements were performed to verify single channel noise temperatures.

4.4 Noise Temperature Comparisons and Hot-Cold Measurements

This section describes our November 2009 Hot-Cold Y-factor measurements as well as other noise temperature comparisons from model and measured data. With the array completed it was necessary to perform whatever tests were available to our location—without a dish to make

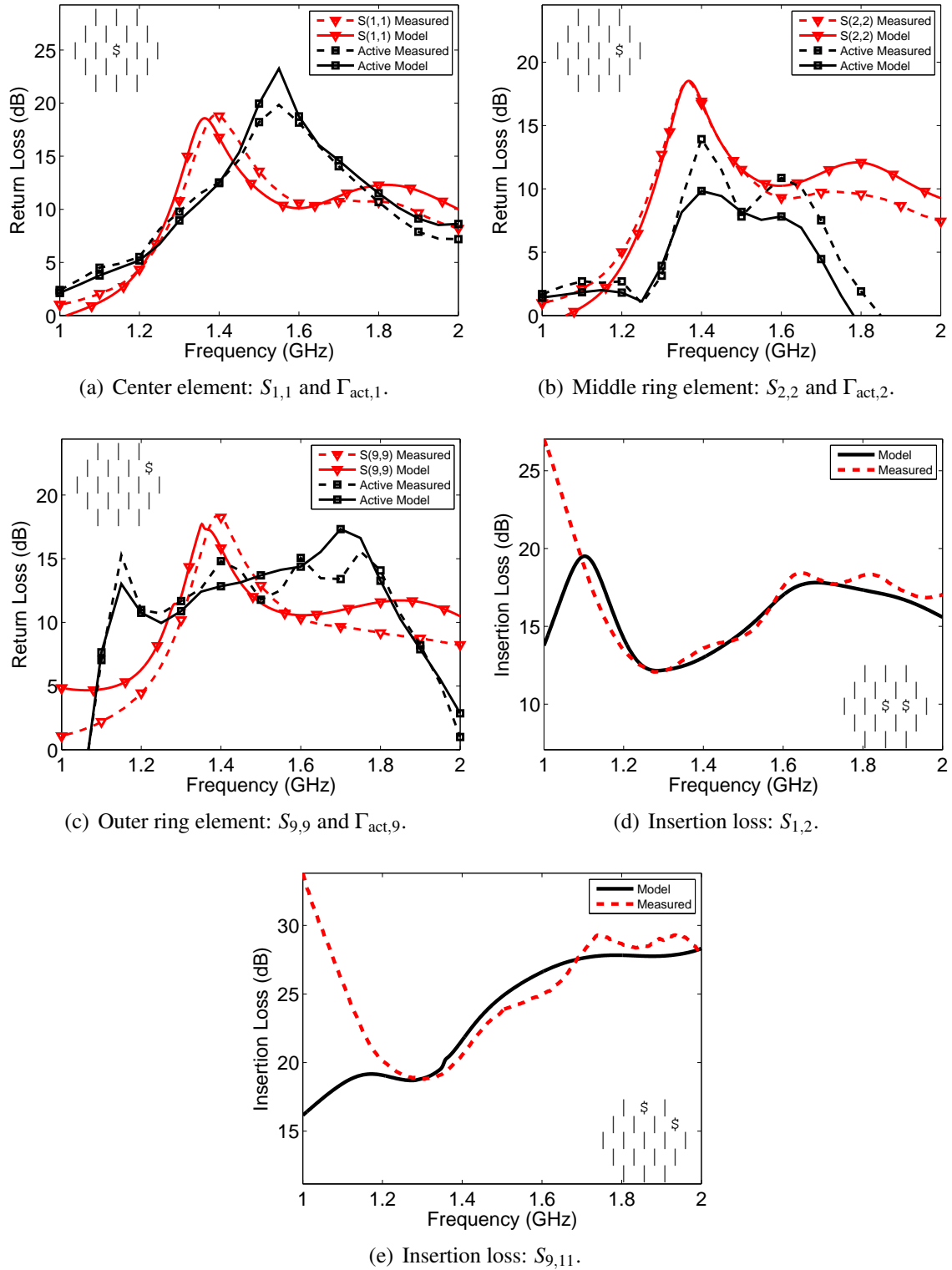


Figure 4.7: Plots of return and insertion loss for several elements, at least one on each ring of the array ($S_{1,1}$, $S_{2,2}$, $S_{9,9}$, $S_{1,2}$, and $S_{9,11}$). Each return loss plot contains losses for self-impedances and active impedances (measured impedances, model fields).

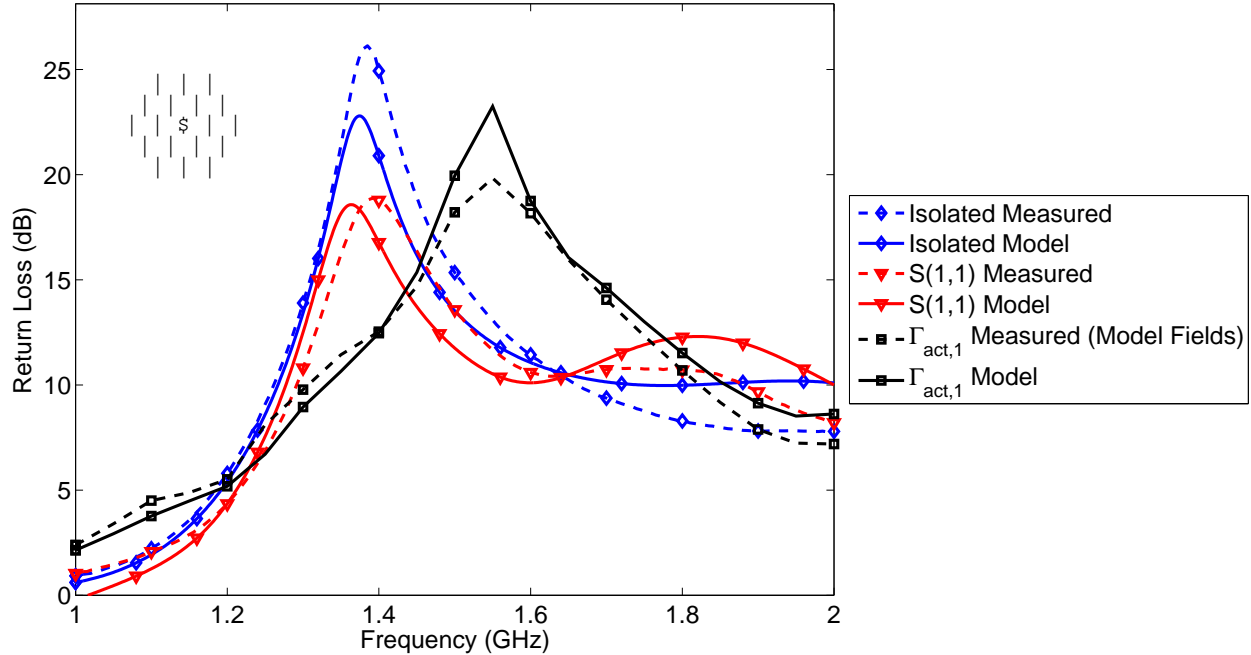
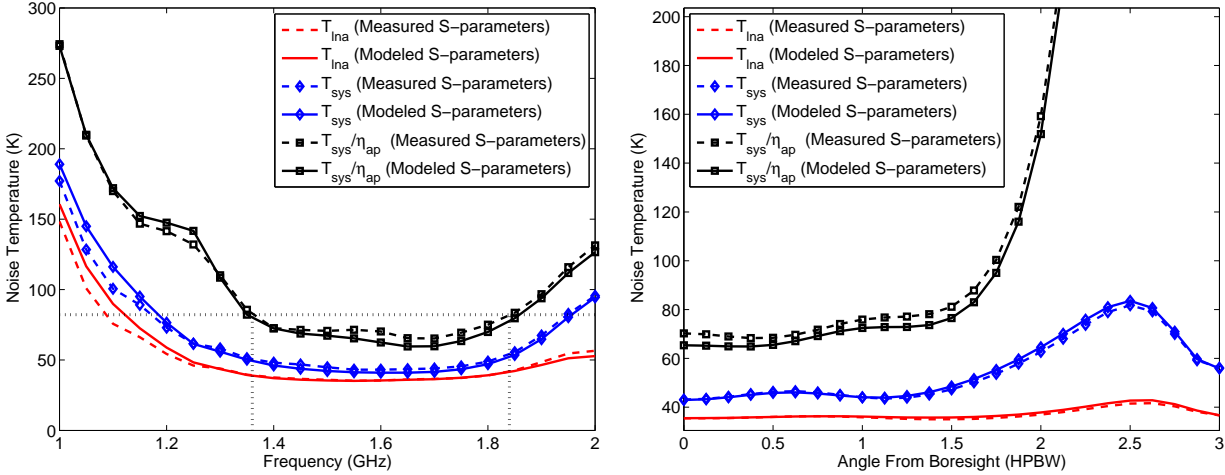


Figure 4.8: Return loss associated the center element of the nineteen element array.

full system measurements and without an anechoic chamber to make fields measurements, the best available option was to measure noise power and system noise temperatures through Y-factor techniques. First, however, system temperatures and efficiencies will be compared from model fields and modeled and measured scattering parameters.

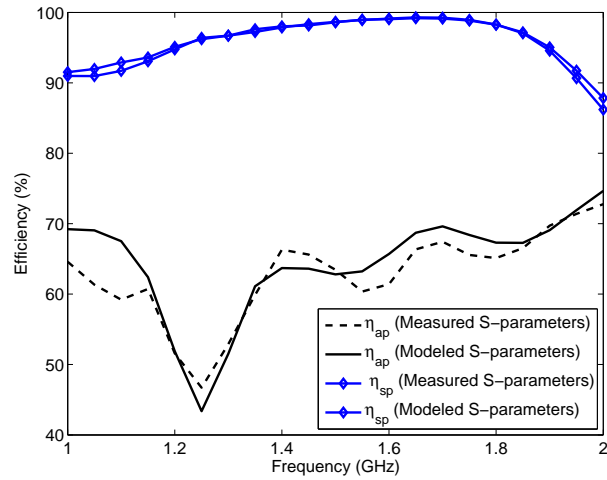
4.4.1 System Noise Temperatures and Efficiencies

Again, utilizing model and measured scattering parameters with model fields provides a means of comparing system temperatures. Figure 4.9(a) displays T_{LNA} , T_{sys} , and T_{sys}/η_{ap} versus frequency over 1-2 GHz, where T_{sys}/η_{ap} is inverse sensitivity normalized with respect to A_{phy} (see Equation 2.31). As expected, T_{sys}/η_{ap} displays the largest noise temperature (due to η_{ap}), while T_{LNA} is the smallest with the fewest contributing components. The overall model 1 dB sensitivity bandwidth of 480 MHz (1.36 GHz to 1.84 GHz) corresponds to the boxed section of Figure 4.9(a) and model and measured curves match well over this section. It is interesting to note the short plateau around 1.2 GHz in T_{sys}/η_{ap} , corresponding to the brief dip in aperture efficiency as depicted by Figure 4.9(c).



(a) Noise temperatures vs. frequency.

(b) Noise temperatures vs. angle from boresight.



(c) Spillover and Aperture efficiencies.

Figure 4.9: System temperature and efficiency plots. As fields had not actually been measured at this point, all ‘measured’ curves incorporate measured scattering parameters with model fields to approximate system noise temperature and efficiency.

Another interesting comparison is that given by Figure 4.9(b) which shows the same parameters against beam steering angle. As expected, steering the beam further from boresight decreases aperture efficiency which in turn drastically increases noise temperature. However, although model and measured curves again match well, understanding of the actual fields and formed beams is required to further characterize and validate the array.

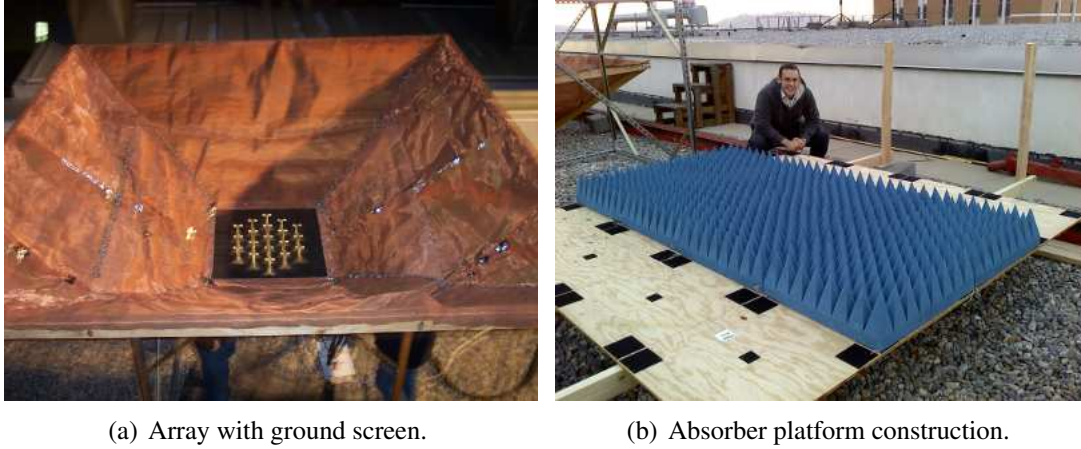


Figure 4.10: These pictures show the construction of an absorber platform and the array attached to a ground screen in preparation for the hot-cold noise measurements.

4.4.2 Hot-Cold Measurements

Y-factor hot-cold measurements were performed on the Clyde building roof utilizing a copper ground screen to block black-body radiation from the ground and other objects typically in the on dish spillover region (see Figure 4.10(a)). With the LNAs, receiver, and data acquisition system connected, ‘cold’ sky measurements were taken by pointing the array toward the sky and turning off any lights and nearby RF instrumentation. Due to the cold blackness of space and scattering from the horizon, we assume a measured RF temperature (T_{cold}) of 7 K (see Section 4.4). ‘Hot’ data was similarly collected by covering the array with an RF absorber platform as seen in figure 4.10(b). RF absorber, as the name implies, absorbs RF radiation and radiates back a noise temperature corresponding to the ambient temperature. As the experiment was performed outside on a cold November night, T_{hot} was assumed to be 270 K (about 26 degrees Fahrenheit).

Because the receiver channel path gains and phases were unknown for this experiment, max-SNR beamformers (or any other multi-channel dependant beams) could not be applied to the data. In order to get a helpful comparison, each channel’s noise temperature was measured by applying a beamformer with every other channel zeroed out and the channel in question multiplied by one (see Section 2.5.1, specifically Equations 2.39, 2.40, and 2.26). Figure 4.11 shows single channel noise temperatures for all 19 elements at 1.6 GHz, as well as points representing the optimal T_{LNA} match from the model and the minimum noise temperature from the LNA itself (a

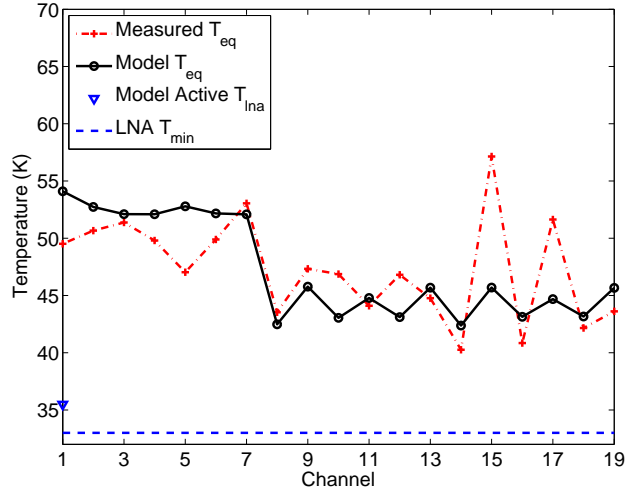


Figure 4.11: Single channel equivalent noise temperatures.

perfect match could theoretically obtain T_{min}). Model and measured results match well - with the exception of channels 15 and 17 where measured channel noises were higher than expected. Most likely these two channels had poor element-LNA junction connections, resulting in degraded performance, or the individual amplifiers have slightly different impedance characteristics resulting in larger noise contributions [30].

4.5 On Dish Array Characterization

The Carter array has been installed and tested on two large reflector dishes: the 300-meter Arecibo radio-telescope (Arecibo, PR) in June and August of 2010 and the 20-Meter dish (Green Bank, WV) in early 2011. The following section describes the array characterization experiments performed at each location and explains the resulting measured figures of merit.

4.5.1 Arecibo Phased Array Feasibility Study

In 2010, the BYU radio astronomy group was contracted by the National Astronomy and Ionosphere Center (NAIC) to perform a study on the feasibility of utilizing phased array feeds on the Arecibo radio-telescope. Located outside of Arecibo, Puerto Rico and measuring 300 meters



Figure 4.12: The Arecibo radio telescope.

in diameter¹, the Arecibo radio-telescope is the worlds largest and most sensitive reflector system in the world (see Figure 4.12). This section briefly describes some of the experimentation work done in Arecibo, with particular emphasis on characterization of the single pol Carter array.

Among the first observations performed, frequency scans provide sensitivity measurements over frequency. Collecting one ‘on’ and one ‘off’ four second pointing in 10 MHz increments from 1.2 to 1.91 GHz, sensitivity was calculated and normalized by physical area as described previously for comparison. As these results are most instructive when compared with other measured data and model results, a more thorough discussion is given in Section 4.5.3.

Ultimately of the highest priority for NAIC, the bulk of our observation time was spent obtaining superfine sensitivity maps. Sensitivity maps, such as that shown in Figure 3.2(b), display sensitivity versus azimuth and zenith angles and provide a measure of how well an array can be electrically steered while still producing accurate results. However, due to spherical dish optics which produce a focal plane rather than focal point, an overlapping series of array positions was required to map the full area.

Using a positioner system designed by David Smith comprised of three motors that move in radius and focus and sweep in angle to position the array around the focal plane, observations were taken at each overlapping position as labeled in Figure 4.13. Resulting sensitivity maps for the

¹It should be noted that the dish optics prohibit utilizing the full surface area for observations. While the full surface area is $7.07 \times 10^4 \text{ m}^2$, only $3.96 \times 10^4 \text{ m}^2$ is illuminated at any given time and this is the value used for calculations throughout this report.

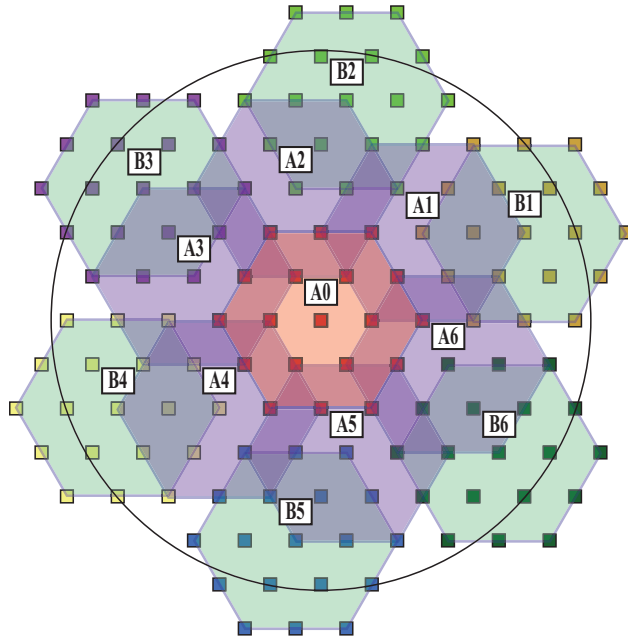


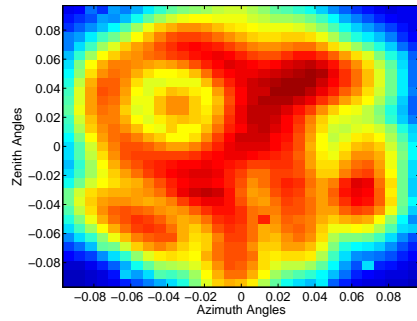
Figure 4.13: The overlapping array positions required to fill Arcicibo's focal plane if looking at the mounted array from below. The labeled hexagons are overlapping array positions A0 through B6, while the squares represent array element positions.

overlapping positions A0 through A6 are shown in Figures 4.14(a) through 4.14(g). It should be noted that because the array positioner rotates the array in angle, each array location actually collects data in a different, though non-orthogonal polarization. However, since astronomical sources are often unpolarized (as they are in this case), there is no preferred array polarization.

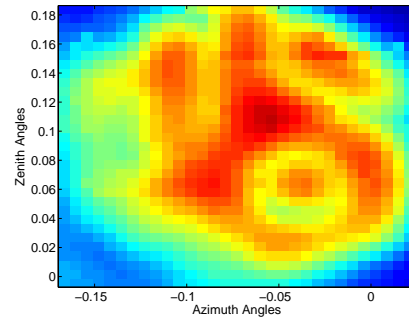
Of particular interest in each sensitivity map is the donut shaped artifact. While no particular cause has yet been determined, we do know that the artifact is not caused by low element SNR, but corresponds to a particular array channel whose signal correlates slightly differently with surrounding elements than other channels. Aberrations such as this are unusual in that they have a definite and symmetric shape and can be repeatedly tied to a particular element location.

4.5.2 20-Meter On Dish Measurements

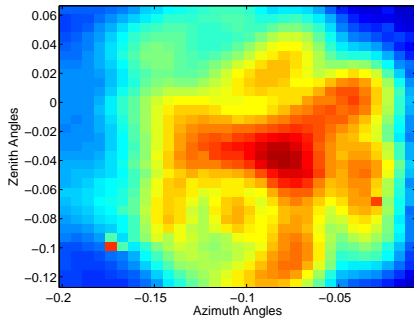
Beginning in January 2011, similar experiments were done on the 20-meter dish at the National Radio Astronomy Observatory (NRAO) in Green Bank, West Virginia. However, since the 20-meter dish uses parabolic optics, multiple array positions were not required. Figure 4.14(h) shows a 23 by 23 pointing sensitivity map obtained with the Carter array in February of 2011. A



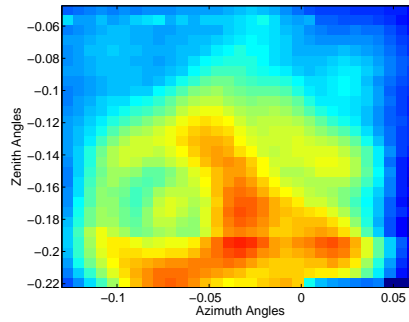
(a) Arecibo A0.



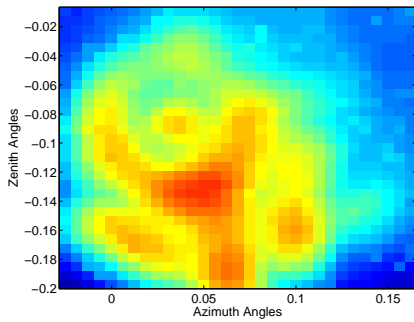
(b) Arecibo A1.



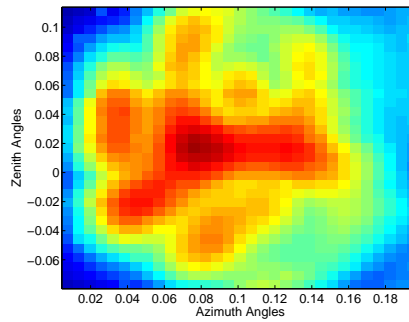
(c) Arecibo A2.



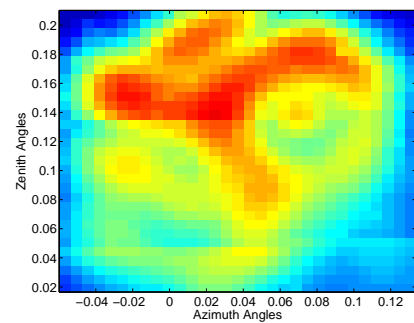
(d) Arecibo A3.



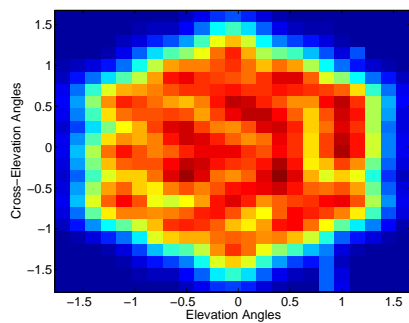
(e) Arecibo A4.



(f) Arecibo A5.



(g) Arecibo A6.



(h) Green Bank 20-Meter.

Figure 4.14: Subfigures (a) through (g) are Arecibo 31x31 superfine sensitivity maps (A0-A6) as measured for the single pol Carter array in June 2010. Subfigure (h) is a 23x23 sensitivity map taken on the 20-Meter dish in Green Bank, WV in February 2011.

brief comparison between the sensitivity map from Green Bank and those from Arecibo shows that observed sensitivities are more evenly distributed with the array setup on the 20-Meter than they were in Puerto Rico. The artifact is gone on the 20-Meter and measured sensitivities appear more as we would expect.

Frequency sweeps were also performed in Green Bank. Data was collected in 20 MHz increments from 1.18 GHz to 2 GHz using the same array setup as for the sensitivity map. As with the Arecibo data, these measurement will be discussed more completely in Section 4.5.3.

4.5.3 Model and On Dish Comparisons

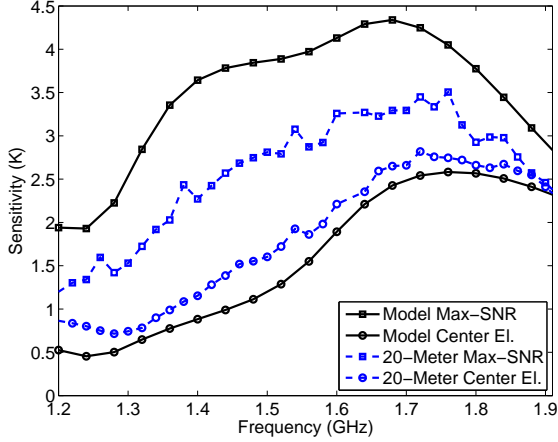
Combining results from the Arecibo and Green Bank experiments as well as data from the model, this section provides an analysis of how well the model matches measured data. Because significant discrepancies between data sets exist, our current understanding of possible problems will also be explained.

Sensitivity and $T_{\text{sys}}/\eta_{\text{ap}}$

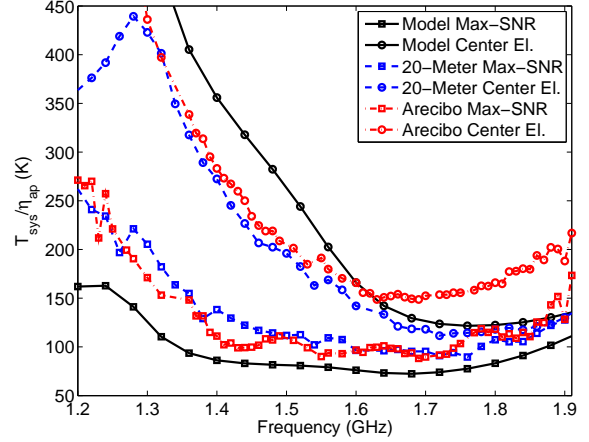
Starting with sensitivity as shown in Figure 4.15(a), the model predicts a high-bandwidth, highly sensitive array for the boresight max-SNR beam (reaching as high as $4.34 \text{ m}^2/\text{K}$ at 1.68 GHz). Unfortunately, max-SNR sensitivity measured on the 20-Meter dish in Green Bank is significantly lower, reaching only $3.51 \text{ m}^2/\text{K}$ at 1.76 GHz². Comparing center frequency (1.6 GHz) results shows measured 20-Meter sensitivity values are only 79% as large as expected, a significant discrepancy.

In order to use Arecibo data for comparison, measured and model sensitivity data was converted to $T_{\text{sys}}/\eta_{\text{ap}}$ by Equation 2.31. The resulting noise temperatures, as shown in Figure 4.15(b), make it apparent that measurements taken in Arecibo correspond well with those from the 20-Meter. Both Arecibo and Green Bank $T_{\text{sys}}/\eta_{\text{ap}}$ measurements are about 79% higher than model predictions at 1.6 GHz. Despite this difference, all three curves have the same general shape suggesting that measured data either has more noise than was accounted for in the model, or measured

²As the physical area of the Arecibo dish is so much larger than the 20-Meter dish (the 20-Meter dish size was assumed in modeling), a side by side comparison of sensitivities between the two does not mean anything. For that reason, Arecibo sensitivity data was left off of Figure 4.15(a), though it is included in Table 4.3 for reference at 1.6 GHz.



(a) Sensitivity for max-SNR and center element only beams (model and 20-Meter).



(b) $T_{\text{sys}}/\eta_{\text{ap}}$ for model and measured max-SNR and center element only beams.

Figure 4.15: Model and measured sensitivity and $T_{\text{sys}}/\eta_{\text{ap}}$ data plots.

Table 4.3: Max sensitivity and minimum $T_{\text{sys}}/\eta_{\text{ap}}$ for the measured and model single pol Carter array at boresight (1.6 GHz).

Data Source	Beam	Sensitivity	$T_{\text{sys}}/\eta_{\text{ap}}$
Model (20 Meter)	Max-SNR	4.13 m ² /K	76.1 K
Model (20 Meter)	Center Element	1.89 m ² /K	166 K
20-Meter	Max-SNR	3.26 m ² /K	96.4 K
20-Meter	Center Element	2.21 m ² /K	142 K
Arecibo	Max-SNR	410 m ² /K	96.7 K
Arecibo	Center Element	239 m ² /K	166 K

efficiencies (aperture, spillover, or radiation) are lower than expected. For comparison in both Figures 4.15(a) and 4.15(b), curves representing sensitivity and $T_{\text{sys}}/\eta_{\text{ap}}$ for the center element only beamformer (see Equation 2.7) have also been included. As the center element beamformer eliminates data from every element but the center, the sensitivity shown is essentially for an embedded single element antenna. In this case, model and 20-Meter data matches well in both plots, though Arecibo measurements do not do as well over the whole bandwidth. Differences between Arecibo and 20-Meter center element beam $T_{\text{sys}}/\eta_{\text{ap}}$, however, is likely due to distinctions in focal plane effects determined by variations in dish optics. Where the parabolic nature of the 20-Meter focuses captured power to a single focal point, Arecibo's spherical optics focus power to a focal

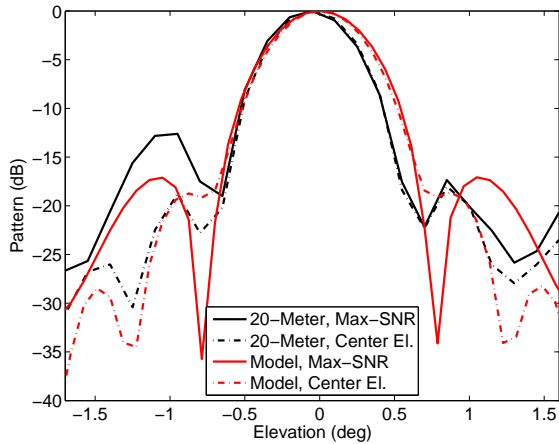
Table 4.4: Model and measured 20-Meter half-power beam width (HPBW) data for the boresight beam.

Data Source	Direction	Beam	HPBW
Model	Elevation	Max-SNR Center Element	0.64 deg 0.60 deg
	Cross-Elevation	Max-SNR Center Element	0.76 deg 0.66 deg
20-Meter	Elevation	Max-SNR Center Element	0.57 deg 0.55 deg
	Cross-Elevation	Max-SNR Center Element	0.67 deg 0.63 deg

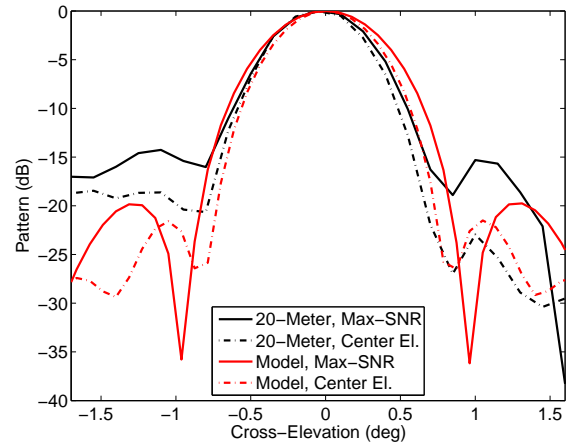
plane. Because the center array element is centered at the focal point on the 20-Meter and at the center of the focal plane at Arecibo, differences in the noise power experienced on the two dishes should be expected. These effects are not as noticeable for full array formed beams, however. For completeness, Table 4.3 provides maximum sensitivity and minimum $T_{\text{sys}}/\eta_{\text{ap}}$ measurements for both Arecibo and 20-Meter measurements as well as model predictions.

Beam Patterns

Beam patterns provide another measurable means of comparison, as differences in patterns can correspond to both η_{ap} and η_{sp} discrepancies. Figures 4.16(a) and 4.16(b) show model and 20-Meter max-SNR and center element only beam pattern cuts. Although nulls and side-lobes are typically at the same angles, model side-lobes are in general 5 dB lower than measured, increasing the overall received system noise. Also of significance, model beams are wider in both elevation and cross-elevation cuts. As per Table 4.4, half power beam widths (HPBW) for measured max-SNR beams are only 88% as wide as model predictions, meaning that the dish is being over-illuminated. This effect can cause several problems, the most important of which being that over-illumination will increase η_{ap} and reduce η_{sp} . Since η_{sp} is more heavily weighted than η_{ap} when it comes to sensitivity, the overall system noise temperature is increased.



(a) 20-Meter and model elevation beam cuts (dB).



(b) 2-Meter and model cross-elevation beam cuts (dB).

Figure 4.16: Measured and model beam pattern cut comparisons.

Analysis of Results

As evidenced in preceding sections, the single pol active matched Carter array underperforms in on dish experimentation. While the exact cause is unknown, this section outlines what is known and provides possible explanations.

Known results and issues. The following is a list of known system issues and details that may stem from an assortment of problems. While not all inclusive, this list describes the most significant findings.

- For all room temperature experiments (including dual pol results explained later), center-element beam SNR is as expected. Since sensitivity is related to SNR by a simple factor, this can be seen directly from the measured center element beam curve of Figure 4.15(a) which matches almost perfectly with model predictions.
- Other single element equivalent noise temperatures from hot-cold experiments agree with the model, assuming T_{cold} equals 7 K.
- Array noise is generally less correlated than expected in the model. This is troublesome because active impedance matching relies on having highly correlated system noise.

- There is no evidence of significant noise reduction due to active impedance matching. This does not mean active impedance matching has not reduced mutual coupling noise, just that we have yet to directly link it to any results.
- For all receivers, data acquisition systems (DAQ), and arrays (again including some dual pol results) the center element gain stays constant.
- Time delays/phase errors in the system must be corrected before correlating. Because DAQ card sampling times can vary over observations (usually around a half sample per channel), resulting time and phase delays must be accounted for in order to get accurate results.

Candidate causes of reduced sensitivity. Although not every potential cause can be derived from what is known about the system, the following list describes the most likely sensitivity reducing issues.

- Active impedance matching was done assuming a particular noise environment. Increased sky noise and/or other unaccounted for noise sources or environmental changes during on dish experimentation could change the beamformer significantly. Said another way, the array may have been actively matched to a beam that does not accurately represent on dish environments.
- Unaccounted for receiver noise could significantly degrade system SNR. While known receiver and DAQ noise temperatures were accounted for (and added very little noise), loose connections and/or variations in individual channel noise contributions would increase the overall system noise. However, since center element beam sensitivity matches model sensitivity and max-SNR beams weight the center element much more heavily than other elements, it is unlikely that significant noise contributions can be attributed to these components. Also, noise contributions of this type would show up in sensitivity maps and, though it is hard to tell from the Arecibo maps, they are not readily apparent in the 20-Meter map of Figure 4.14(h).
- As noted in Section 4.5.3, narrower measured beam patterns and higher side-lobes as well as scattering from parts of the dish itself would increase spillover noise and reduce the quan-

tity of received signal. Typically, narrow beam patterns that over illuminate the dish are indicative of poor element patterns, but center element results imply that this is not the case.

- Another possibility, should spillover efficiency not be the issue, is that aperture efficiency is low. While in Section 4.5.3 it was shown that beam patterns are somewhat more narrow than expected, it is possible that in many instances they are too wide and the dish is being under-illuminated. However, this issue would also typically be a result of poor element patterns which, as mentioned above, is not the situation.
- Although elements were modeled as perfect electrical conductors, constructed elements were made from brass and plated with copper ($\approx .25$ mil) and gold ($\approx .1$ mil). While copper and gold are very conductive, variations in thickness with respect to skin depth as well as unavoidable sharp edges and unsmooth machined surfaces could add several Kelvin to the system temperature and reduce η_{rad} . Like previous issues though, this problem is unlikely in view of center element results since the center element beam works well and the center element was made the same as any other element.

Again, the preceding list provides some of the most educated guesses as to why the single pol Carter array underperforms, but is not meant to be exhaustive. At the time of writing, discussion with NRAO and on-going experimentation on the 20-Meter continues to narrow the field of causes.

4.6 Summary

This chapter has discussed the design and characterization of a single polarization phased array feed for radio astronomy. Several element types were tested before the ‘Green Bank balun’ model was selected and fully modeled from isolated elements on a ground-plane to a full nineteen element hexagonal array. Elements were active matched to a max-SNR boresight beam and constructed from gold plated brass. Scattering parameter measurements for isolated and embedded elements matched model predictions as per Figures 4.6, 4.7, and 4.8. Using hot-cold Y-factor noise measurement techniques along with measured scattering parameters and model fields, single element equivalent noise temperatures (T_{eq}) and best estimate system noise temperatures (T_{sys}) were calculated and again found to match well with the model (see Figures 4.9 and 4.11). Finally, arrays

were fully characterized on reflectors in Arecibo, PR and in Green Bank, WV. On dish results show the array underperforming in overall sensitivity and, while the exact cause of measured and model figure of merit discrepancies are unknown, a discussion of known significant details and probable causes was given in Section 4.5.3 and will be continued to some extent in Chapter 5 with dual pol results.

CHAPTER 5. DUAL POLARIZATION ARRAY FEED DESIGN

This chapter details the development of a new optimization process and several dual polarization phased arrays. As all previous BYU radio astronomy array design was with single polarization, moving to dual polarized arrays represents a big step in both model size and data analysis complexity. For simplicity, all array models made and described herein utilize crossed-dipole elements where antennas of both polarization are centered at the same location—while other types of dual polarization arrays were analyzed, we found it most convenient and time efficient to model and analyze arrays with only one co-located hexagonal grid. The following section describes an updated method for optimizing phased array feeds.

5.1 Infinite Array Model and the Matlab Optimizer

While the methods described in Section 4.2 worked well for the single pol Carter array design, there are two fundamental weaknesses with this method defined below and described in more detail in the following subsections:

1. As arrays increase in complexity and size, optimization slows down significantly. Depending on the version of software and complexity of the model, each iteration of the seven element Carter array took one hour while a nineteen element array required four hours to complete on an eight-core Mac Pro computer with 32 Gigabytes of RAM.
2. As outlined in Section 4.2, because beamformers were calculated only once per optimization, resulting PAFs were actually optimized to another arrays max-SNR beamformer. In essence, this method prevents the design of truly optimal arrays in the max-SNR sense (although the Carter array came close).

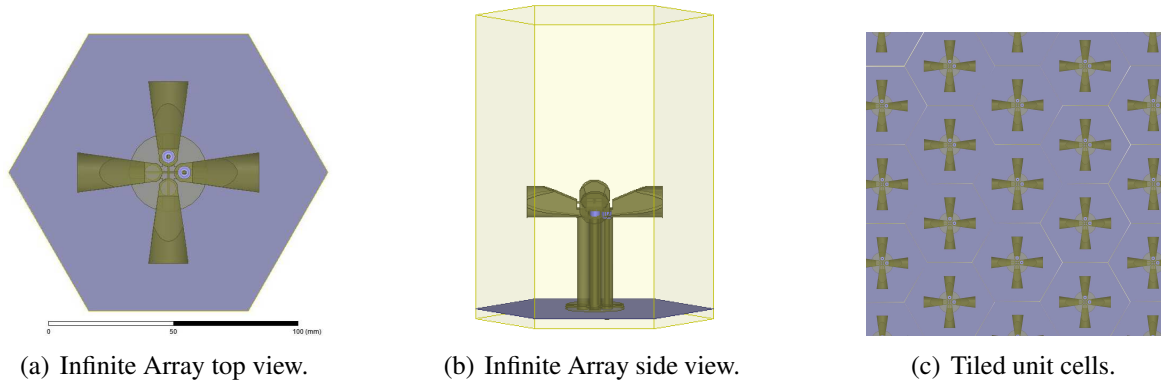


Figure 5.1: Infinite array unit cell.

5.1.1 Increasing Modeling Efficiency and the Infinite Array Model

As noted, array modeling can become extremely time intensive. Because dual pol arrays essentially contain twice the components of their single pol counterparts, it became necessary to either reduce the complexity of each model file or find ways to speed up simulations of the full array. While both techniques were eventually used to reduce array design time, perhaps the most significant improvement came from implementing an infinite array model.

Infinite Arrays

Infinite array models effectively mimic array designs with an infinite number of elements equally spaced across a plane using only a single, repeatable unit cell. Although our array is not actually infinite in size, the most significant element (center) is surrounded by several rings of antennas and can be effectively modeled by an infinite environment. The unit cell itself is defined by boundaries in the shape of the cell (hexagon) that take in incident fields and act as though those fields then enter the cell from the opposite side of the antenna—as though they had come from a neighboring antenna with similar cell shape and excitation. An example of an infinite array cell structure can be seen in Figures 5.1(a) and 5.1(b). These images show a single dual pol element over a small hexagonal patch of ground-plane that reflects the size and shape of one cell within our hexagonal array grid. Similarly, Figure 5.1(c) depicts what a section of the array would look like if a unit cell were tiled into a true infinite array.

Because infinite arrays require only one cell and provide embedded active impedances (essentially every element in the infinite array is weighted equally), the savings in time is enormous even though this method was only used to provide an appropriate starting point for a finite array optimization.

Other Time Reducing Measures

Besides infinite arrays, optimization time was also reduced in the following ways:

- A new, faster computer was purchased and used in tandem with previous devices. The new system, a Mac Pro with dual four core processors and 32 GB RAM, allowed multiple, separate optimizations utilizing an assortment of algorithms to run simultaneously on several machines. Typically, two to three variations of a model were optimizing on any given computer, depending on array size.
- The version of commercial software used was completely revamped twice, making it run more quickly and efficiently.
- Multi-core processing techniques were utilized.

Together these methods reduced optimization iteration times from one hour for the seven element single pol array to approximately forty minutes for an equivalent fourteen element dual pol array. In both cases arrays were implemented with a single ring of single or dual pol elements around the center. Similarly, while a nineteen element single pol array previously took around four hours, a thirty-eight element dual pol array required only three to three and a half hours.

5.1.2 The Matlab Optimizer

In order to address the issue of changing fields/beamformers between optimization iterations as mentioned above, a new approach was taken to independently optimize the software model array through in-house, non-commercial codes. Written primarily by Taylor Webb with direct contributions from David Carter, the Matlab optimizer also provides an assortment of cost functions and optimization algorithms not available previously. The following paragraphs describe how the Matlab optimizer operates.

After choosing a parameterized array model, center frequency¹, and optimization algorithm, the Matlab optimizer allows users to input any choice of array parameters and their ranges, as defined in the model, to include in the optimization space. A cost function definition (i.e.: cost = $T_{\text{sys}}/\eta_{\text{ap}}$), noting that the optimizer's objective is to minimize cost, is also necessary before the optimization will function correctly.

Once initiated, the optimizer calls our modeling software, inputs new parameter dimensions depending on the chosen optimization algorithm, and starts a simulation. After the simulation completes, fields and impedances are extracted and used to compute figures of merit (active impedances, T_{LNA} , T_{sys} , η_{sp} , η_{ap} , sensitivity, etc.) which are then input into the cost function. Because these values are calculated every iteration, the correct max-SNR beamformers can then be applied to each model which in turn avoids the changing fields issue discussed previously. Ideally, by repeating this process hundreds of times, as required by the cost function and optimization algorithm, and utilizing the model with lowest cost, we can produce an acceptably optimized array.

5.2 Dual Polarization Element Designs

This section describes modeled dual pol array variations as well as data from those that were constructed. However, at the time of writing full dual pol data is limited because of difficulties with receiver systems dropping data and array cabling. What results are available will be presented in the appropriate sections.

As we moved to dual pol element design, problems with the structural integrity of the single pol elements, specifically the joint where dipole arms solder to balun posts and coax lines (see Figure 4.1.3), led to the design of new arm/post joints and ground-plane connection plates. This was done with help from BYU PML personnel and several BYU manufacturing engineering students. The new design implements a small metal lip on each dipole arm with a cylindrical groove that rests on and is soldered to the arm's post, strengthening their mechanical connection. Also, grooves were added to the ground-plane connection plate for more convenient arm alignment. These changes can be seen in the dipole designs of Figure 5.2.

¹As of the latest array model these codes only provided optimization at a single frequency point.

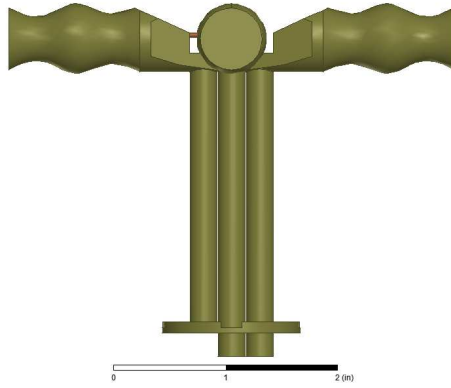
Of the several dipole designs that were looked at, three models were developed enough to be used within the Matlab optimizer. These three models were called the ‘spline’ dipole, the ‘ear’ dipole, and the dual pol ‘kite’ dipole.

5.2.1 Spline Dipoles

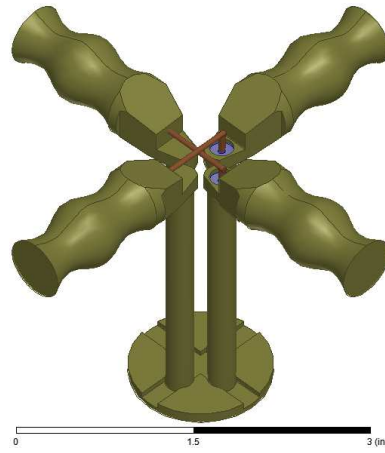
As the most radical design, spline dipoles get their name from the technique used to design their arms. Utilizing a spline curve with five adjustable points in one plane, each arm was defined by sweeping the spline around an axis and joining the then three dimensional object with support posts using a small metal lip as described previously. The concept of the spline arm came from a desire to provide as many optimizable parameters as possible to produce the desired active impedance match. Eventually, eleven parameters were optimized in the final iteration of spline dipoles, namely the separation between arms and the ground-plane, the lengths of cuts in the sides and top of the arms, the radius of the feed line, the length of the spline part of the arms, the length of the non-spline part of the arms, and the vertical positions of the five adjustable spline points. Despite having the most optimizable parameters of any design, spline dipole optimizations never obtained sensitivity values as large as other designs. In all likelihood this worked for the best, as spline arm shapes would be difficult and expensive to manufacture. An example of the spline arm is shown in Figures 5.2(a) and 5.2(b).

5.2.2 Ear Dipoles

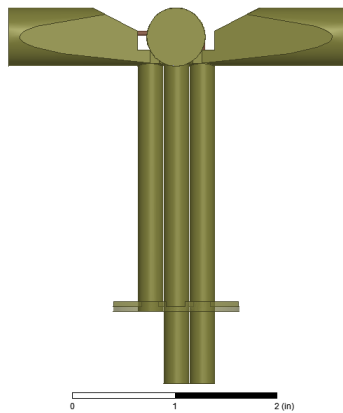
Ear dipoles were the first fully optimized and constructed dual pol elements. Named for the lip or ‘ear’ that supports the arms, ear dipoles were the first to implement the new arm support structure. As seen in Figures 5.2(c) and 5.2(d), ear dipoles have standard thickened dipole cylindrical arms, but with cuts on the top and sides for matching. Unlike spline elements, ear elements have only six optimizable parameters: arm length, dipole radius, separation between the ground and dipole arms, the length of the cut on the side of dipole arms, the length of the cut on the top of dipole arms, and feed line radius. Despite this, ear dipoles outperformed spline elements in the Matlab optimizer. Modeled sensitivity and active impedance plots for a 38 element array of ear elements are given in Figure 5.3.



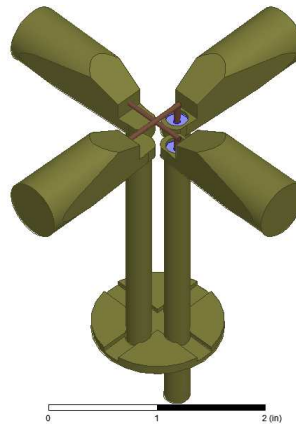
(a) Dual pol spline element side view.



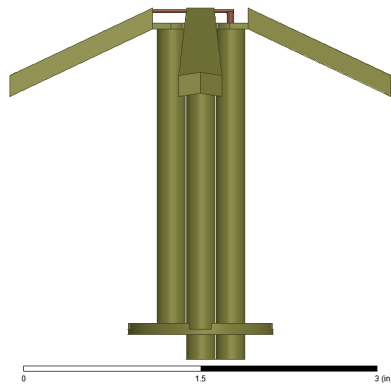
(b) Dual pol spline element above-diagonal view.



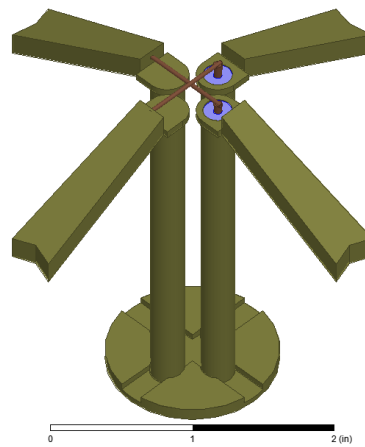
(c) Dual pol ear element side view.



(d) Dual pol ear element above-diagonal view.

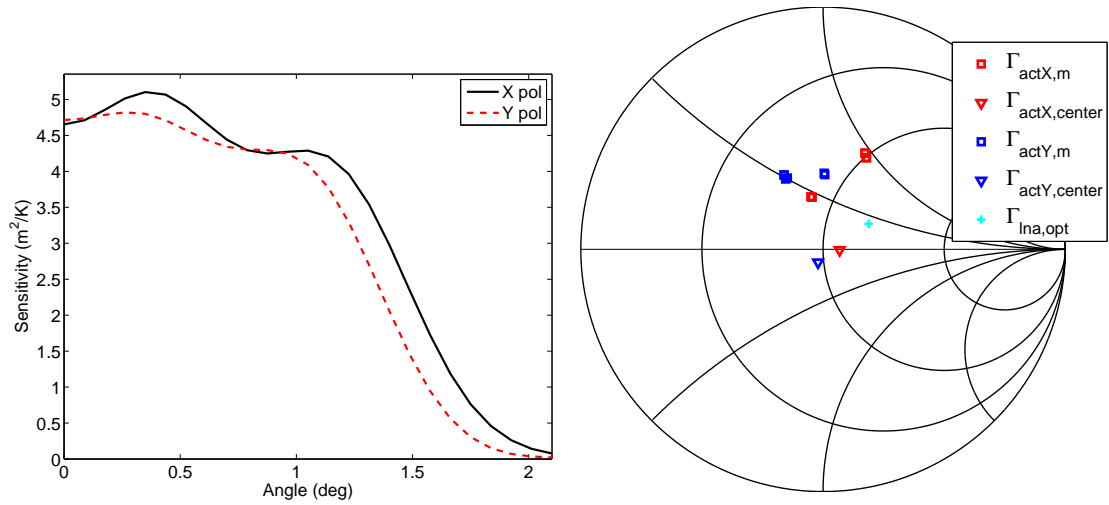


(e) Dual pol kite element side view.



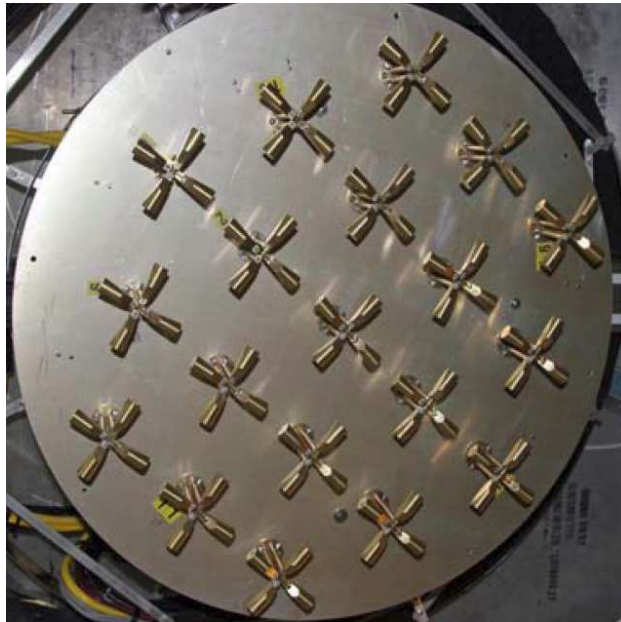
(f) Dual pol kite element above-diagonal view.

Figure 5.2: Top and side views of the spline, ear, and cryo kite dual pole element models.



(a) Optimal ear dipole sensitivity vs. angle.

(b) Ear dipole Γ_{act} for the center and first ring elements.



(c) Ear dipoles on ground plane as mounted in Arcibo.

Figure 5.3: Modeled sensitivity and active impedance plots for dual pol ear elements. The bottom picture shows ear dipoles mounted on a ground-plane in Arcibo, PR [31].

In May-June 2010, a thirty-eight element ear array was constructed by the BYU PML from machined brass and shipped to the Arecibo observatory for use in our June/August 2010 Arecibo experiments. As mentioned previously, receiver errors prevented full array characterization, but what was done is presented in Section 5.3.

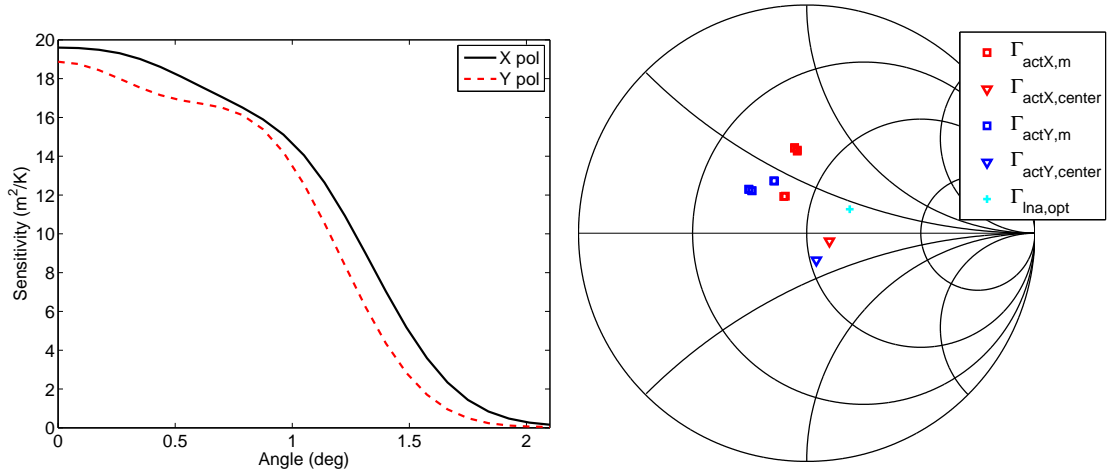
5.2.3 Cryo Kite Dipoles

The dual pol kite element was initially optimized as a possible replacement for the ear dipole array in the summer of 2010. Based off the original single pol kite model and updated with a more structurally sound support system, the dual pol kite utilized seven optimizable parameters: the kite length from feed to outside corner, the kite length from feed to center corner, kite thickness, the separation from ground-plane to feed point, the angle between feed axis and kite outside corner, the angle between support posts and dipole arms, and feed line radius. As can be seen in Figures 5.2(e) and 5.2(f), these optimization parameters (specifically the angle between support posts and dipole arms) allow dipole arms to bend up or down from the feed line axis to provide bandwidth support as well as increased matching capabilities. In terms of optimized sensitivity from the Matlab optimizer, the dual pol kite outperformed all other dual pol arrays.

As originally designed, the dual pol kite was never built. However, at the time of its optimization NRAO started work on a liquid helium (cryo) cooled phased array system and the dual pol kite was chosen as its array element. Modifications were necessarily made to the element's base-plate and connector system (a push-on variation of the standard SMA connector was used) and simulations showed no degradation in performance, so an array was constructed to model specifications. Model sensitivity and active impedance plots for dual pol kite elements with cryo-cooled LNAs can be seen in Figure 5.4.

5.3 Experimental Results

This section details results for the two dual pol arrays described previously. Most measured results are either based on data from a single polarization of elements within the array, or dual polarizations from only the center rings of elements due to circumstances mentioned previously.



(a) Optimal cryo-kite sensitivity vs. angle from the model. (b) Cryo-kite Γ_{act} for the center and first ring elements.



(c) Cryo-kite as mounted in Green Bank, WV.

Figure 5.4: Modeled sensitivity and active impedance plots for cryo kite elements. The bottom image shows cryo-kite elements mounted on a ground-plane in Green Bank, WV.

5.3.1 Ear Dipole Results

The dual pol ear array was used only temporarily at the Arecibo Observatory in June and August 2010. Unfortunately, the 40 channel receiver system used to collect data malfunctioned repeatedly during this time, requiring us to use a smaller 20 channel system. Because of this, all data presented here was taken with only half of the elements connected—usually one set of polarized elements or a smaller ring of dual pol elements. To differentiate, one polarization was

called pol 'A', and the other pol 'B'. Also, since the ear dipole was used on the Arecibo telescope, the array was moved around the focal plane in positions described by Figure 4.13.

Although no frequency sweeps were performed, multiple calibration grids on known sources were taken using the ear array at the center frequency, 1.6 GHz. Figure 5.5 shows an assortment of sensitivity maps from observations made throughout June and August 2010. The first three images (Figures 5.5(a) through 5.5(c)) are superfine, 31x31 grids done at array positions A4, A5, and A6 using array elements of polarization 'A'. Figures 5.5(d) through 5.5(h) are fine 15x15 grids, ranging in both array position and element polarization. These images provide examples of how each polarized element responds to sources at various array positions. Regrettably, similar grids were never collected for comparison with the same array position and oppositely polarized element using the full 19 elements per polarization. There were, however, two grids taken at the A0 array position with the center ring of both polarization elements connected.

An important element of dual pol array analysis is a comparison of each polarization's sensitivity and patterns as well as the instrument polarization efficiency for a particular beam (max-SNR in this case). While a complete analysis of this data is pending in future work by Taylor Webb and others of the BYU radio astronomy group, Figure 5.6 breaks down the two mentioned A0 fine grids that include both polarizations in the following way:

- Subfigures 5.6(a) and 5.6(e) show the original dual pol 15x15 grids with 19 array elements. Each grid includes 7 elements of each polarization in the center and first element ring, as well as 5 additional elements at three locations on the outer ring that give the images their triangular shape.
- Subfigures 5.6(b) and 5.6(f) depict the same 15x15 grids as before, but with the 5 outer ring elements ignored. This was done due to inconvenient element ordering in the saved correlation files that made it impossible to determine which of the 5 elements corresponded to each polarization.
- Subfigures 5.6(c) and 5.6(g) show sensitivity maps made from the portion of data corresponding to elements with polarization 'A'.
- Subfigures 5.6(d) and 5.6(h) depict sensitivity maps made from the portion of data corresponding to elements with polarization 'B'.

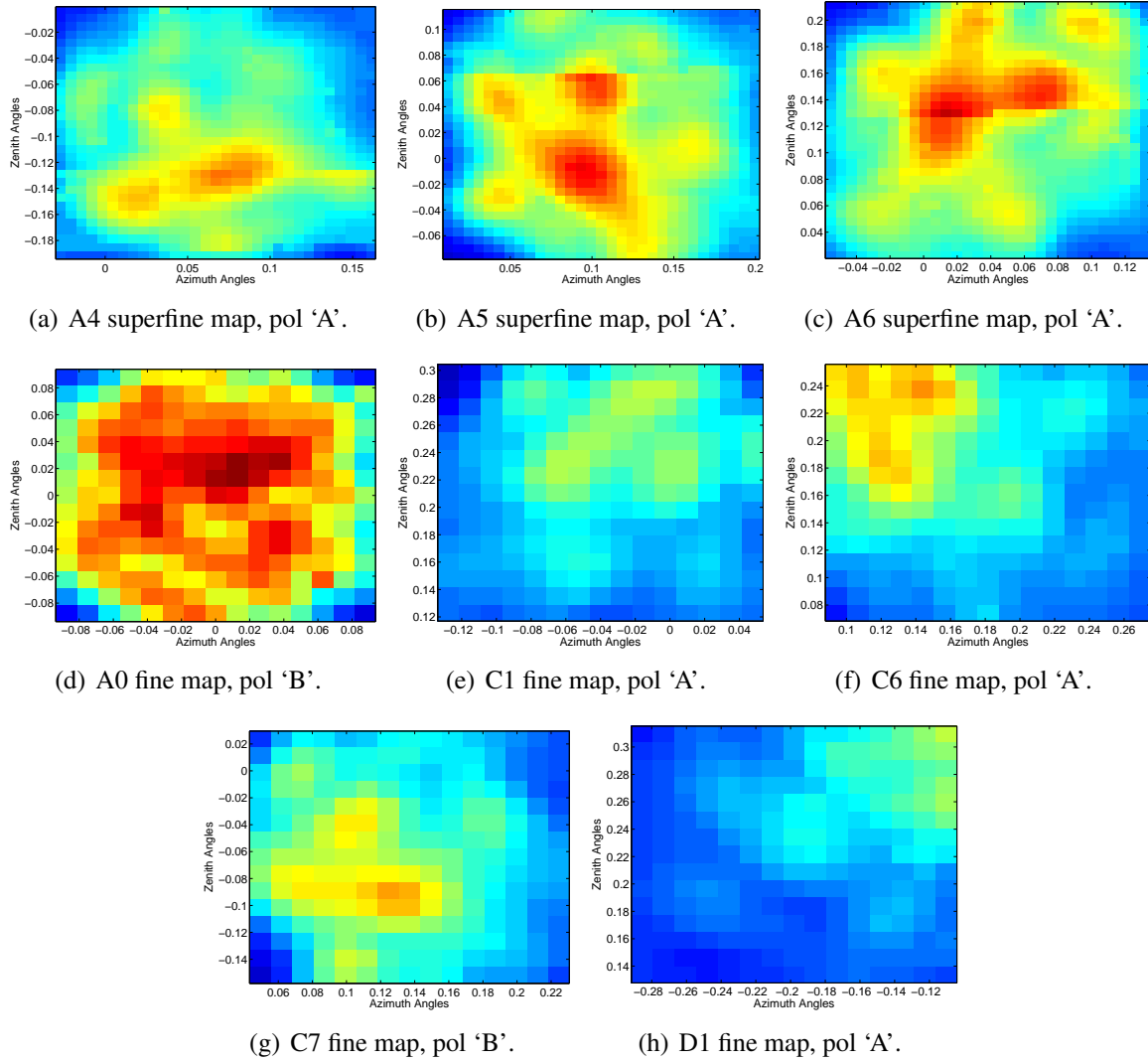


Figure 5.5: Dual polarization ear element sensitivity maps using one polarization or the other. For array positions, see Figure 4.13.

Comparing 'A' and 'B' pol maps provide two interesting insights for the ear array. First, 'A' maps have an odd symmetry with high sensitivities in the top right and bottom left portions of the center hexagon, while 'B' maps have almost all of their highest values in the hexagon's upper half. Secondly, 'B' pol sensitivities were generally larger in magnitude across the map. While 'A' pol grids contain an average of 49.5 pointings with sensitivities above 60% of the maximum measured 7 element single pol value, 'B' pol grids of the same size contain an average of 57 pointings of that

Table 5.1: Maximum sensitivities for the dual pol ear array using 19 and 7 element single pol, and 14 element dual pol variations at boresight and array position A0. All data at 1.6 GHz.

Data Source	Polarization	Figure	Sensitivity	$T_{\text{sys}}/\eta_{\text{ap}}$
Measured maximum 19 element, single pol	‘B’	5.5(d)	436 m ² /K	90.9 K
Model maximum 19 element, single pol	‘B’	NA	502 m ² /K	79.0 K
Measured maximum 14 element, dual pol	‘AB’	5.6(b)	409 m ² /K	96.9 K
Model maximum 14 element, dual pol	‘AB’	NA	444 m ² /K	89.2 K
Max measured 7 element ear array, single pol	‘B’	5.6(d)	400 m ² /K	98.9 K
Other measured 7 element ear array, single pol	‘A’	5.6(g)	396 m ² /K	100 K

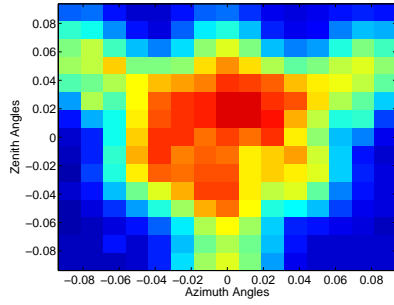
magnitude. The direct cause of these differences is currently unknown, but may be contributed to slight differences between the separately polarized elements or lack of polarimetric calibration.

Of the sensitivity maps of Figure 5.6, the largest sensitivity attributed to the ‘A’ polarization for the max-SNR beam is 396 m²/K. Similarly, the largest sensitivity for the ‘B’ polarization is 404 m²/K. Including the sensitivity maps of Figure 5.5, the overall maximum sensitivity value measured on the dual pol ear array is 436.2 m²/K (found on the full 19 element ‘B’ pol array in the A0 array position)—in terms of noise temperature, this value is equivalent to a $T_{\text{sys}}/\eta_{\text{ap}}$ of 90.9 K. Unfortunately, 19 element measured sensitivity is 15% lower than corresponding model values as per Table 5.1 (measured 7 element are 8% low).

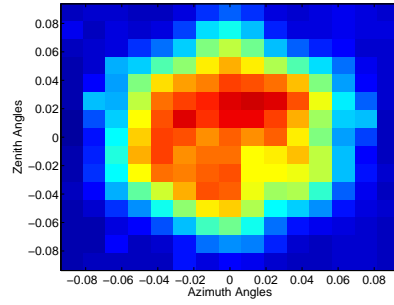
These variation in measured and model sensitivity are likely due to element losses and poorer than expected aperture or spillover efficiencies. However, as the model was simulated using codes designed for NRAO’s 20-Meter dish applied to Arecibo’s tertiary reflector (they have similar focal length to diameter ratios), there may have been errors when determining model noise. Another source of error may be poor original element construction. When the ear elements were first returned from the shop, very few were correctly aligned so that when mounted on a ground-plane they all pointed in different directions. This fabrication flaw undoubtedly disrupted our carefully tuned impedance match and increased T_{rec} .

5.3.2 Cryo Kite Results

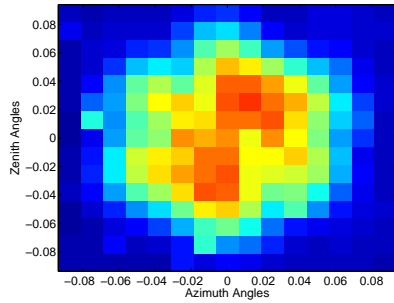
In April through May 2011, the cryo cooled dual pol kite array was mounted on the 20-Meter dish in Green Bank, WV. Regrettably, as of this writing only enough cable was run for data



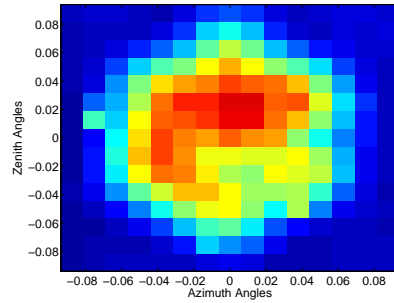
(a) A0 fine map, center rings and three outer ring elements, pols 'A' and 'B'.



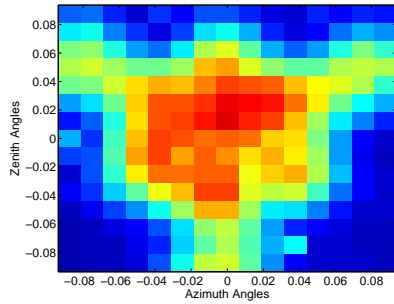
(b) A0 fine map, center rings, pols 'A' and 'B'.



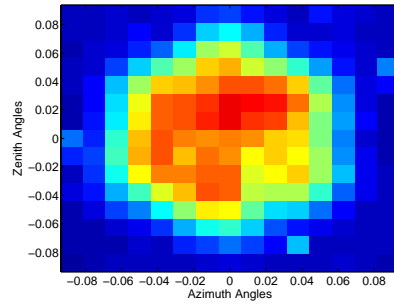
(c) A0 fine map, center rings, pol 'A'.



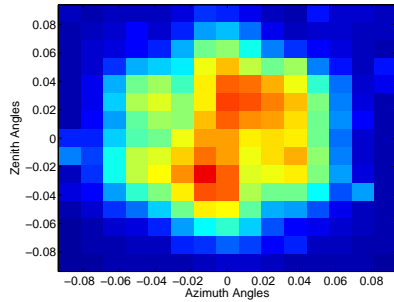
(d) A0 fine map, center rings, pol 'B'.



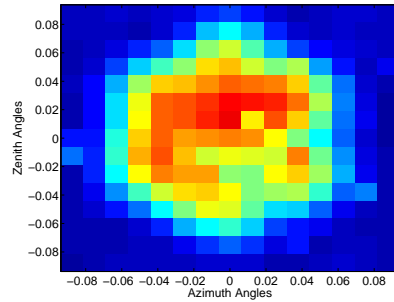
(e) A0 fine map, center rings and three outer ring elements, pols 'A' and 'B'.



(f) A0 fine map, center rings, pols 'A' and 'B'.



(g) A0 fine map, center rings, pol 'A'.



(h) A0 fine map, center rings, pol 'B'.

Figure 5.6: Dual polarization ear element sensitivity maps with both polarizations. Channels were filtered by polarization in each map so that individual polarization sensitivities could be compared. For array positions, see Figure 4.13.

collection from 19 array elements. Because of this, all data sets herein are essentially 19 channel single pol, or 19 channels distributed among the two element polarizations on the inner rings of the array².

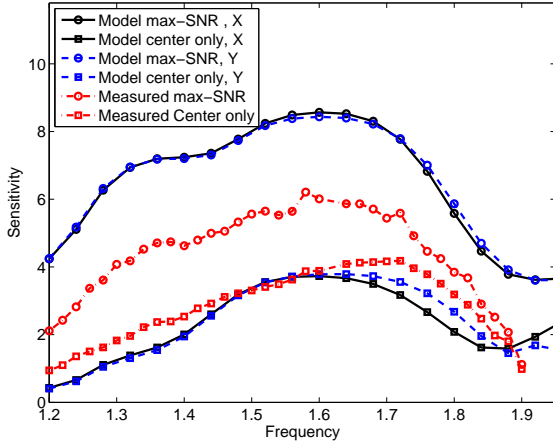
Several frequency sweeps were performed on the cryo kite array: a 20 MHz increment sweep from 1.2 to 1.9 GHz and a 1 MHz increment sweep from 1.60 to 1.64 GHz. A comparison of measured and modeled sensitivity and $T_{\text{sys}}/\eta_{\text{ap}}$ for the 20 MHz sweep are shown in Figures 5.7(a) and 5.7(b). It should be noted that model T_{sys} was modified from the ideal values assumed in Figure 5.4(b) to more realistic values by increasing the assumed T_{sky} from 3 to 5 K, applying 4 K of T_{loss} , adding an additional 5 K of T_{sp} for scattering off the dish support structure, and including 3.6 K of loss for the stainless steel transition between dipole and cryo cooled LNA. Still, measured sensitivity is 29% lower than expected given the added noise contributions; measured $T_{\text{sys}}/\eta_{\text{ap}}$ is 12 K higher than model predictions over most of the band. However, despite not reaching sensitivity goals, the array still manages an adequate 1 dB bandwidth of 306 MHz.

Hot-Cold Analysis

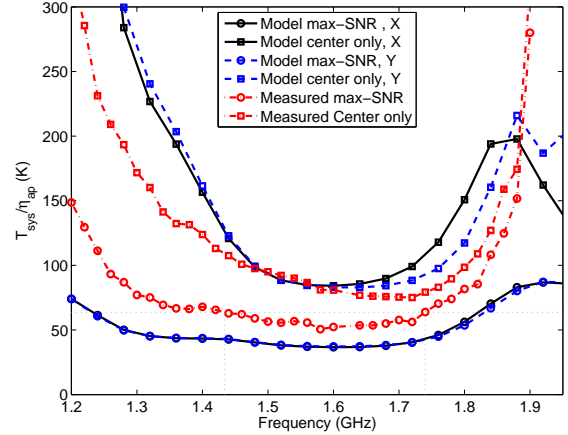
A hot-cold, Y-factor test was performed on the cryo kite array in June 2011. As shown in Figure 5.8, measured curves roughly follow model shapes, but remain several Kelvin higher. Model and measured values for isolated elements follow closely from 1.3 to 1.4 GHz, but separate over the rest of the bandwidth by approximately 2 K. Embedded element measurements are further separated, particularly at higher frequencies where Y pol elements have a much higher T_{eq} , but come close at 1.64 GHz with only 2 K separation. A curve of T_{min} and coaxial measurements for T_{LNA} are also given for reference, [32].

The fact that model and measured T_{eq} curves do not line up suggests that there are still some unaccounted for noise terms. As we have assumed only 4 K of T_{loss} (see Table 5.8(d)), it may be that brass elements are more lossy than expected. Brass is about one fourth as conductive as copper, though they are both very highly conductive metals and it was assumed little loss would result from using the more easily machined brass. Another possibility is that there is actually more loss in the cryo transition than expected. Because the LNAs are liquid helium cooled, a stainless

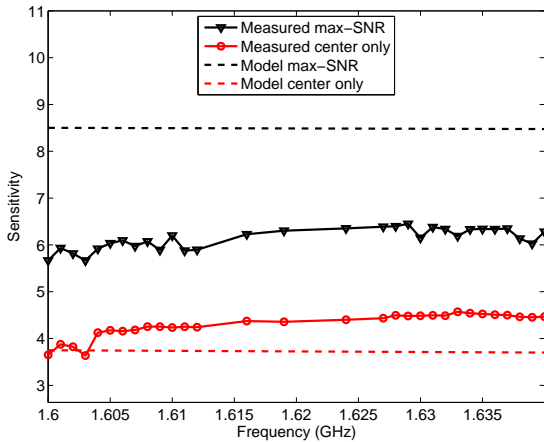
²As there are only 14 element locations between the inner ring and center element, these measurements usually included 5 outer ring elements.



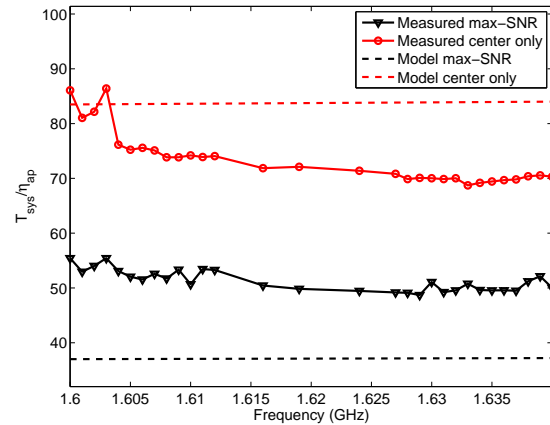
(a) Cryo kite measured and model sensitivity.



(b) Cryo kite measured and model $T_{\text{sys}}/\eta_{\text{ap}}$ with approximately 306 MHz of 1 dB bandwidth.



(c) Cryo kite measured sensitivity in 1 MHz increments.



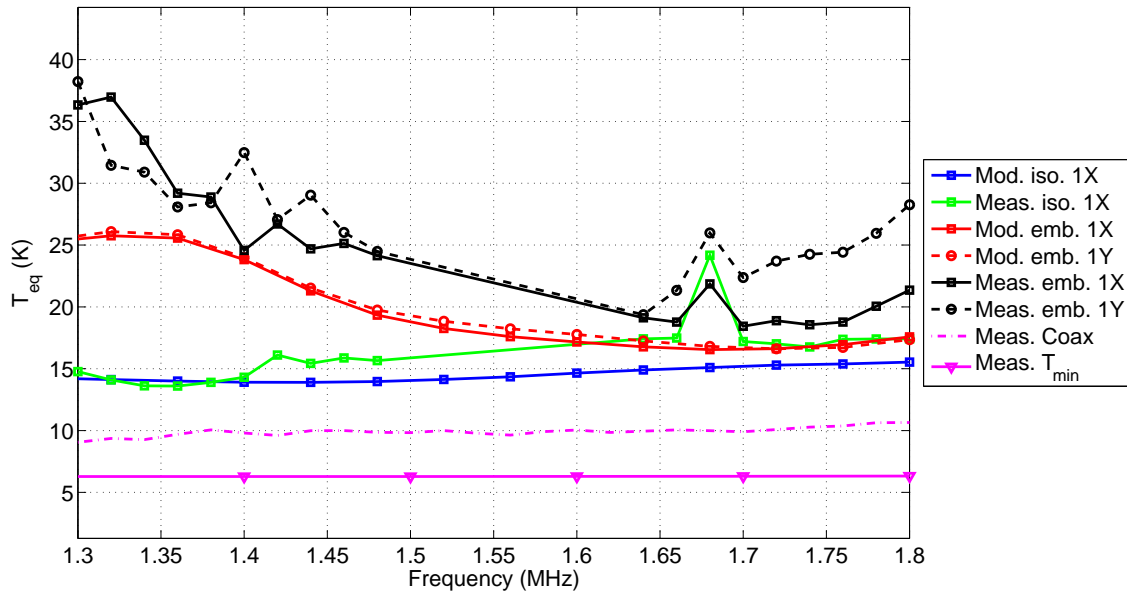
(d) Cryo kite measured $T_{\text{sys}}/\eta_{\text{ap}}$ in 1 MHz increments.

Figure 5.7: Model and measured sensitivity and $T_{\text{sys}}/\eta_{\text{ap}}$ plots for cryo kite elements.

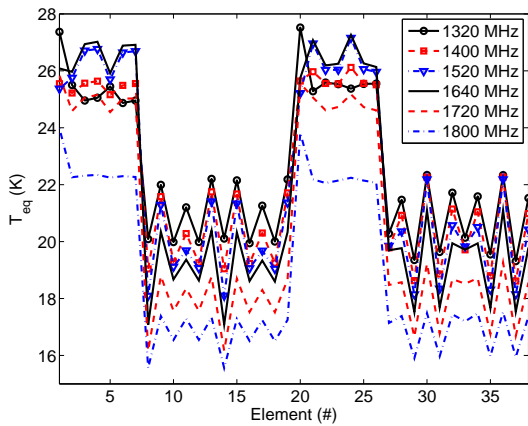
steel transition was required to move from the cryo cooled area to array elements. Assuming the array is perfectly matched makes the transition noise temperature (T_{tran}) equal to the coaxial measurements minus T_{min} , which is approximately 3.6 K in this case.

Single Pol Observation Grids

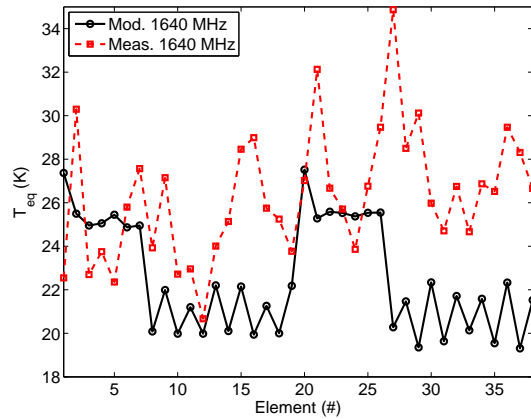
As with the ear array, single polarization calibration grid observations were taken with the cryo kite array, but on the 20-Meter dish in Green Bank. Figure 5.9 presents four, 19 channel



(a) T_{eq} over frequency.



(b) Model T_{eq} over channel.

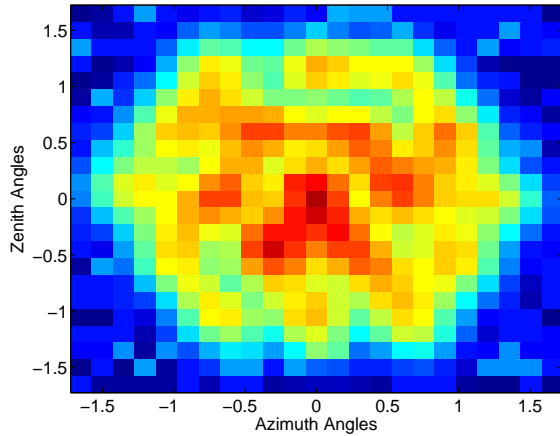


(c) Model and measured T_{eq} over channel at 1.64 GHz.

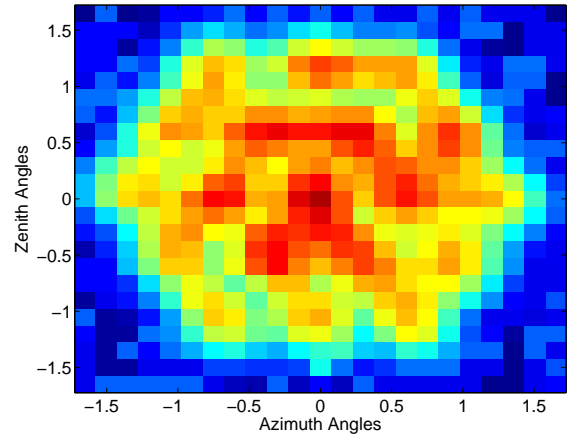
Noise Term	Temperature
T_{LNA}	9.8 K
T_{loss}	4.0 K
T_{tran}	3.6 K

(d) Model noise budget table at 1.64 GHz.

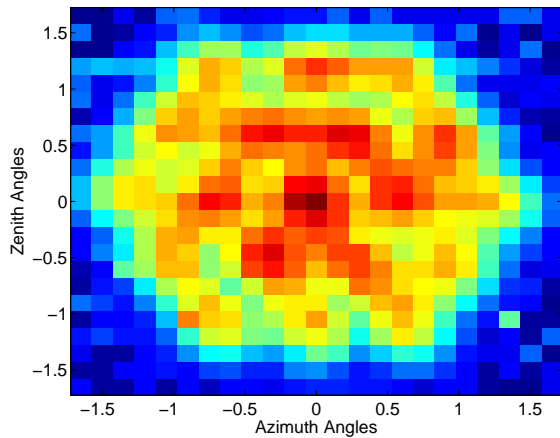
Figure 5.8: Results from the hot-cold, Y-factor test performed in June 2011. In Subfigure 5.8(a), ‘iso’ stands for isolated and represents a single dual pol element on ground-plane. Similarly, ‘emb’ stands for embedded and represents an array with all element on the ground-plane, but only one element connected without beamformer. Table 5.8(d) displays noise budget information for the model.



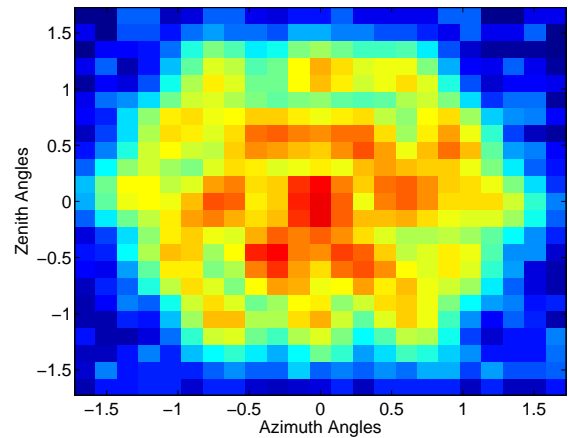
(a) Calibration grid, May 16.



(b) Calibration grid, May 16.



(c) Calibration grid, May 17.



(d) Calibration grid, May 18.

Figure 5.9: Full, 23x23 observation grids on CasA using the ‘X’ polarization element of the cryo kite array.

single pol grids utilizing the ‘X’ polarized element³. Large amounts of RFI required moving the observation frequency of these sensitivity maps from 1.60 GHz to 1.64 GHz, though this did not affect performance. At boresight the maximum sensitivity measured was $6.46 \text{ m}^2/\text{K}$ —somewhat higher than seen in the frequency sweep ($5.87 \text{ m}^2/\text{K}$)—but still 23% lower than predicted by the model. As per Table 5.2, this measured sensitivity corresponds to a $T_{\text{sys}}/\eta_{\text{ap}}$ of 48.6 K.

One interesting feature of these sensitivity maps when compared with those taken in Arecibo using the ear array is the clarity and consistency of sensitivity values. Admittedly, these grids were

³While element polarizations were labeled ‘A’ and ‘B’ on the ear array in Arecibo, ‘X’ and ‘Y’ were used for the cryo kite array in Green Bank.

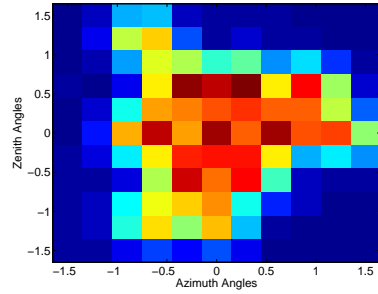
all taken at a single array position since Green Bank’s dish optics do not require larger focal area coverage. Still, compared with Arecibo’s center A0 grids, these sensitivity maps are particularly clear as to element locations. Elements in the center and first ring are especially easy to spot as the dish steers across the sky.

Dual Pol Observation Grids

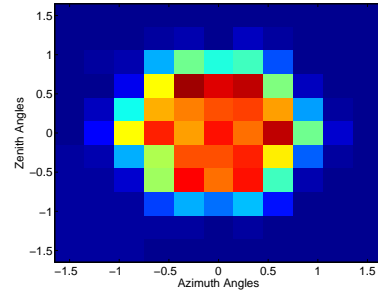
Figure 5.10 depicts several dual pol calibration grids obtained with the cryo kite array on May 21, 2011. Similar to the dual pol ear data, these images show data sets with the center and first ring elements of both polarizations connected, as well as several second ring elements (through all second ring elements are ‘X’ polarization for this setup). In the cryo kite case, ‘Y’ pol elements outperformed ‘X’ pol by 24% in number of pointings with sensitivities larger than 60% of the maximum measured 7 element single pol value. As per Table 5.2, the largest measured sensitivity measured with the inner 7 elements of both polarizations was $5.32 \text{ m}^2/\text{K}$. With only ‘X’ pol elements connected, sensitivity dips to $5.16 \text{ m}^2/\text{K}$, but reaches as high as $5.29 \text{ m}^2/\text{K}$ with ‘Y’ elements. Corresponding $T_{\text{sys}}/\eta_{\text{ap}}$ values are also included in the table.

Analysis of Results

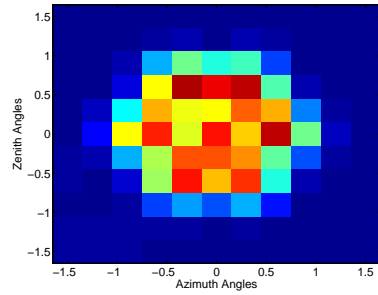
Unfortunately, the cryo kite array did not fully meet expectations. Discrepancies in hot-cold T_{eq} imply that there is at least one underestimated or unaccounted for noise term, but not one significant enough to account for a 15 K difference in formed-beam $T_{\text{sys}}/\eta_{\text{ap}}$. Engineers at NRAO, where the array was mounted, noted two possible noise sources related to element design: material choice and center conductor stability. Although brass is quite conductive, they estimated that by copper and gold plating the center conductor and machining the rest from copper we could reduce ohmic noise by 3 K (4.5 K in $T_{\text{sys}}/\eta_{\text{ap}}$). Also, because the center conductor is not held in place except by friction with the Teflon beads, some noise is likely added by varying crossover gap sizes from the optimal specification (the gap between center conductors at the feed where they cross over each other). The next iteration of feed design should include provision to fix the center conductors axially, eliminating this problem [33].



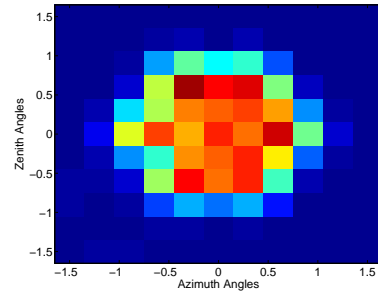
(a) Full 11x11 grid data.



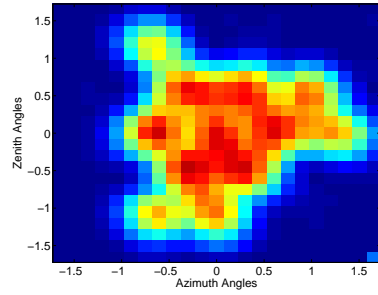
(b) 'X' and 'Y' pol center elements from 11x11 grid.



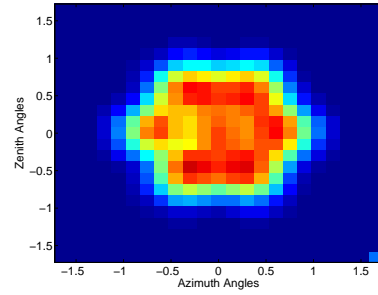
(c) 'X' pol center elements from 11x11 grid.



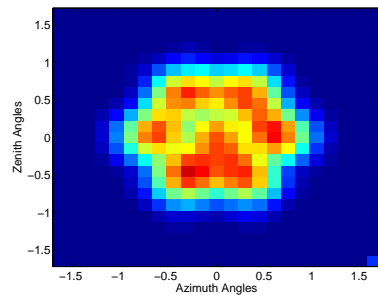
(d) 'Y' pol center elements from 11x11 grid.



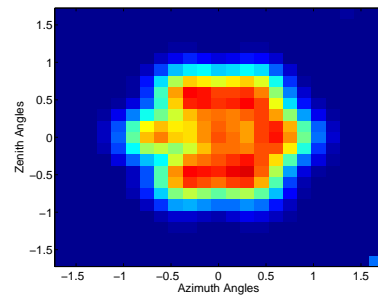
(e) Full 23x23 grid data.



(f) 'X' and 'Y' pol center elements from 23x23 grid.



(g) 'X' pol center elements from 23x23 grid.



(h) 'Y' pol center elements from 23x23 grid.

Figure 5.10: Dual pol data sets from cryo kite array using the same polarization breakdown as Figure 5.6. Subfigures 5.10(a) through 5.10(b) are derived from a 11x11 grid, while Subfigures 5.10(e) through 5.10(f) come from a 23x23 grid. Both observations taken May 21, 2011.

Table 5.2: Maximum sensitivities for the dual pol cryo kite array using 19 and 7 element single pol, and 14 element dual pol variations at boresight. All data at 1.64 GHz.

Data Source	Polarization	Figure	Sensitivity	$T_{\text{sys}}/\eta_{\text{ap}}$
Measured maximum 19 element, single pol	‘X’	5.9(c)	6.46 m ² /K	48.6 K
Model maximum 19 element, single pol	‘X’	NA	8.51 m ² /K	36.9 K
Measured maximum 14 element, dual pol	‘XY’	5.10(b)	5.32 m ² /K	59.1 K
Model maximum 14 element, dual pol	‘XY’	NA	6.58 m ² /K	47.7 K
Maximum 7 element ear array, single pol	‘Y’	5.10(d)	5.29 m ² /K	59.4 K
7 element ear array, single pol	‘X’	5.10(c)	5.16 m ² /K	60.9 K

Despite the potential noise contributions mentioned above, the most likely explanation for low sensitivity is lower than expected aperture or spillover efficiencies from under or over illumination of the dish. At present steps are being taken to test this hypothesis, but no experimental results are as of yet available.

5.4 Summary

This section described the development of dual polarization phased arrays for radio astronomy. Several optimization methods were explored, including infinite array models and the Matlab optimizer. Three antenna designs were also described: the spline dipole which was never built, the ear dipole, and the cryo kite dipole.

The ear dipole array was constructed in May-June 2010 for use at the Arecibo Observatory. Due to an assortment of technical difficulties and lack of time on dish, ear dipoles were never completely characterized as a 38 element dual pol array. From what data was taken, the ear array displayed a sensitivity 15% lower than expected for 19 elements of a single polarization. Possible explanations for array underperformance include additional element ohmic loss, lower than expected aperture efficiency, differences in model and actual system dish optics, and poor element construction resulting in impedance mismatches.

Constructed for NRAO use on the 20-Meter dish, the cryo kite dipole array was assembled in early 2011. Like the ear array, the cryo kite array was never fully characterized on dish, but was employed in 19 single pol element or 14 dual pol element observations. However, both frequency sweeps and a hot-cold analysis were performed for the cryo kite array and resulting data sets were

compared with model values. The cryo kite array also underperformed, displaying a maximum measured sensitivity of $6.46 \text{ m}^2/\text{K}$, 23% lower than expected. Unaccounted for or underestimated noise as well as low aperture or spillover efficiency are the most likely explanations for reduced performance, but have yet to be verified.

Despite these problems, the cryo kite array is the most sensitive low noise PAF ever built for radio astronomy. As the first phased array to utilize a liquid helium cryo-cooling system for on dish observations, the cryo kite's 48.6 K measured $T_{\text{sys}}/\eta_{\text{ap}}$ is significantly lower than any other PAF in existence. These contributions provide astronomers considerable gains in terms of survey speed and sensitivity and ensure the cryo kite's influence in PAF design throughout the radio astronomy community.

CHAPTER 6. CONCLUSION AND FUTURE WORK

This thesis has described BYU contributions to the next generation of low noise phased arrays for radio astronomy. Both single and dual polarization phased array dipoles were developed and implemented in hexagonal grids of 19 and 38 elements for large dish astronomical observation. A complete list of array elements modeled and constructed can be seen in Table 2.2.

Unfortunately, of the three implemented arrays described—the single pol Carter array, the dual pol ear array, and the dual pol cryo kite array—none fully matched model expectations. Lower than expected aperture and/or spillover efficiency, additional ohmic loss, and other noise sources have been described as the most likely culprits. However, with the exception of the Carter array which had narrower than expected beam patterns resulting in low spillover efficiency, none of these have yet been proven.

Despite the challenges and problems associated with these arrays and their implementation on dish, they have each demonstrated significant contributions to PAF design and radio astronomy capabilities. Notable decreases in overall system noise temperature were achieved through active impedance matching and sensitivity optimization techniques developed and actualized as described in Chapters 4 and 5 of this report. The cryo kite array, in particular, has been demonstrated as the lowest noise phased array ever built for radio astronomy. The Carter and ear arrays, on the other hand, were instrumental in proving the feasibility of using phased arrays at the Arecibo observatory.

6.1 Future Work

The first step towards future array development is to fully characterize dual pol arrays and modify model codes to incorporate accurate ohmic loss models and spillover noise due to dish scattering. With more exact models, active matching methods will become more efficient and require less computation time. Also, a better understanding of the polarimetric effects associated

with dual polarized elements in phased arrays will allow astronomers to utilize PAFs for more complex source observations.

Developing an adequate array design for NRAO's 100-meter Green Bank Telescope (GBT) is a challenge currently being met by other members of the BYU radio astronomy group. With a significantly different focal length to diameter ratio than the 20-Meter and utilizing offset dish parabolic optics, multiple changes to current array implementations (including element separation) will be required. New elements will also require the implementation of lower loss materials to reduce loss and some sort of support structure to fix the center conductor axially in place for designs similar to the cryo kite.

Future array element designs are under consideration that incorporate low-noise amplifiers at the feed, rather than behind the ground-plane. This new feature will eliminate balun and transmission line losses between elements and LNA's, but requires the inclusion of complex LNA component shapes for each element into the model during optimization and will be extremely difficult to implement within a cryostat. While increasing model complexity, this step could significantly reduce T_{sys} .

REFERENCES

- [1] J. D. Kraus, *Radio Astronomy*, 2nd ed. Cygnus-Quasar Books, 1986. 1
- [2] R. Giovanelli *et al.*, “The Arecibo Legacy Fast ALFA Survey. I. Science Goals, Survey Design, and Strategy,” *The Astronomical Journal*, vol. 130, no. 6, p. 2598, 2005. [Online]. Available: <http://stacks.iop.org/1538-3881/130/i=6/a=2598> 1
- [3] L. Staveley-Smith *et al.*, “The Parkes 21 cm Multibeam Receiver,” *Publications of the Astronomical Society of Australia*, vol. 13, no. 3. 1
- [4] B. Jeffs, K. Warnick, J. Landon, J. Waldron, D. Jones, J. Fisher, and R. Norrod, “Signal Processing for Phased Array Feeds in Radio Astronomical Telescopes,” *Selected Topics in Signal Processing, IEEE Journal of*, vol. 2, no. 5, pp. 635–646, oct. 2008. 1
- [5] C. K. Hansen, “Beamforming Techniques and Interference Mitigation Using A Multiple Feed Array For Radio Astronomy,” Master’s thesis, Brigham Young University, 2004. 1, 2
- [6] B. Veidt and P. Dewdney, “A Phased-Array Feed Demonstrator For Radio Telescopes,” in *URSI General Assembly*, 2005. 2
- [7] T. Oosterloo, M. Verheijen, and W. van Cappellen, “The Latest On APERTIF,” in *ISKAF2010 Science Meeting*, 2010. 2
- [8] S. Hay, J. O’Sullivan, J. Kot, C. Granet, A. Grancea, A. Forsyth, and D. Hayman, “Focal Plane Array Development for ASKAP (Australian SKA Pathfinder),” in *European Conference On Antennas And Propagation*, Nov 2007. 2
- [9] W. van Cappellen and L. Bakker, “APERTIF: Phased Array Feeds for the Westerbork Synthesis Radio Telescope,” in *Phased Array Systems and Technology (ARRAY), 2010 IEEE International Symposium on*, oct. 2010, pp. 640–647. 2
- [10] A. Chippendale, J. O’Sullivan, J. Reynolds, R. Gough, D. Hayman, S. Hay, R. Shaw, and R. Qiao, “Chequerboard Phased Array Feed Testing for ASKAP,” BYU Phased Array Workshop, Brigham Young University, Provo, UT, 2010. 2
- [11] C. Hansen, K. Warnick, B. Jeffs, J. Fisher, and R. Bradley, “Interference Mitigation Using a Focal Plane Array,” *Radio Science*, vol. 40, June 2005. 2
- [12] J. Nagel, K. Warnick, B. Jeffs, J. Fisher, and R. Bradley, “Experimental Verification of Radio Frequency Interference Mitigation With a Focal Plane Array Feed,” *Radio Science*, vol. 42, Dec 2007. 2
- [13] D. Jones, “Characterization of a Phased Array Feed Model,” Master’s thesis, Brigham Young University, 2008. 2, 5, 21, 32

- [14] J. S. Waldron, “Nineteen-Element Experimental Phased Array Feed Development and Analysis of Effects of Focal Plane Offset and Beam Steering on Sensitivity,” Master’s thesis, Brigham Young University, 2008. 2, 21
- [15] J. Nagel, “A Prototype Platform For Array Feed Development,” Master’s thesis, Brigham Young University, 2006. 2, 21
- [16] K. Warnick and M. Jensen, “Effects of Mutual Coupling on Interference Mitigation With a Focal Plane Array,” *Antennas and Propagation, IEEE Transactions on*, vol. 53, no. 8, pp. 2490–2498, Aug 2005. 3
- [17] K. F. Warnick and M. A. Jensen, “Optimal Noise Matching for Mutually Coupled Arrays,” *IEEE Transactions on Antennas and Propagation*, vol. 55, no. 65, June 2007. 3
- [18] R. Maaskant and E. Woestenburger, “Applying the Active Antenna Impedance to Achieve Noise Match in Receiving Array Antennas,” in *IEEE Antennas Propagation International Symposium*, June 2007, pp. 5889–5892. 3
- [19] K. Warnick, B. Woestenburger, L. Belostotski, and P. Russer, “Minimizing the Noise Penalty Due to Mutual Coupling for a Receiving Array,” *IEEE Transactions on Antennas and Propagation*, vol. 57, no. 6, pp. 1634–1644, June 2009. 3, 6, 8, 13
- [20] H. L. Van Trees, *Optimum Array Processing*, 1st ed. Wiley, 2002. 7
- [21] “IEEE Standard Definitions of Terms for Antennas,” *IEEE Std 145-1993*, p. i, 1993. 10
- [22] D. Roddy, *Satellite Communications*, 4th ed. McGraw-Hill, 2006. 11
- [23] K. F. Warnick and M. A. Jensen, “Antennas and Propagation for Wireless Communications,” ECEn 665 Lecture Notes, Brigham Young University, Provo, UT, 2011. 11
- [24] K. Warnick and B. Jeffs, “Efficiencies and System Temperature for a Beamforming Array,” *IEEE Antennas and Wireless Propagation Letters*, vol. 7, pp. 565–568, 2008. 11
- [25] ———, “Gain and Aperture Efficiency for a Reflector Antenna With an Array Feed,” *Antennas and Wireless Propagation Letters, IEEE*, vol. 5, no. 1, pp. 499–502, Dec. 2006. 12
- [26] K. F. Warnick, M. V. Ivashina, R. Maaskant, and B. Woestenburger, “Unified Definitions of Efficiencies and System Noise Temperature for Receiving Antenna Arrays,” *IEEE Transactions on Antennas and Propagation*, vol. 58, no. 6, pp. 2121–2125, June 2010. 12, 15
- [27] D. M. Pozar, *Microwave Engineering*, 3rd ed. Wiley, 2005. 13
- [28] R. Norrod, Personal Communication, 2010. 16
- [29] J. Landon, M. Elmer, J. Waldron, D. Jones, A. Stemmons, B. Jeffs, K. Warnick, F. J.R., and R. Norrod, “Phased Array Feed Calibration, Beamforming and Imaging,” *The Astronomical Journal*, vol. 139, pp. 1154–1167, March 2010. 24
- [30] K. F. Warnick, D. Carter, T. Webb, J. Landon, M. Elmer, and B. D. Jeffs, “Design and Characterization of an Active Impedance Matched Low Noise Phased Array Feed,” *IEEE Transactions on Antennas and Propagation*, 2010. 41

- [31] G. Cortes, "AOPAF: Arecibo Observatory Phased Array Feed," National Astronomy and Ionosphere Center, Cornell University, Ithaca, NY, 2010. 59
- [32] R. D. Norrod, J. R. Fisher, B. D. Jeffs, and K. F. Warnick, "Development of Cryogenic Phased Array Feeds for Radio Astronomy Antennas," in *IEEE International Symposium on Phased Array Systems and Technology (ARRAY)*, Oct 2010. 66
- [33] R. Norrod, Personal Communication, 2011. 70